esa

ECMWF

ESA Contract Report

PEARL Cloud contract 4000128669/19/NL/CT

Contract Report to the European Space Agency

Assimilation system preliminary assessment for additional EarthCARE observations: Doppler velocity, cloud extinction, Rayleigh backscatter

WP-5000 report

Preparations for EarthCARE Assimilation - Radar and Lidar Cloud Observations (PEARL Cloud)

Authors: Mark Fielding and Marta Janisková

Contract officer: Tobias Wehr

April 2022

ABSTRACT

The report provides a preliminary assessment of the potential for additional EarthCARE observations — those in addition to cloud radar reflectivity and lidar attenuated cloud backscatter — to be included in the ECMWF data assimilation system for monitoring and potential assimilation. The main additional observations considered are radar Doppler velocity, lidar Rayleigh backscatter and lidar cloud extinction. The potential information content of each observation type will be discussed with reference to the Jacobians of the observation operators, which provide the sensitivity of the simulated observations to changes in the model state. Next, the impact of the new observation types will be investigated using single-cycle single-observation-type assimilation experiments. Investigating the impact of assimilating lidar cloud extinction will be taken further through a one-month Observing System Experiment (OSE), where cloud extinction is included in one-month of cycling assimilation experiments. Finally, the potential for observation quality monitoring of solar radiances is discussed.

Contents

1 Introduction

The Earth, Clouds, Aerosols and Radiation Explorer (EarthCARE; Illingworth et al., 2015) satellite will host a range of instruments, all optimised for improving our understanding of the interactions between clouds, aerosols and radiation. Over the past few years, it has been shown, with increasing confidence, that the cloud radar reflectivity and total lidar backscatter observations made by EarthCARE could have a direct impact on numerical weather prediction (NWP) forecasts if they are used in data assimilation (Janisková and Fielding, 2020; Fielding and Janisková, 2020b,c) to help initialise forecasts. Also, as global atmospheric models begin to resolve convective-scale features (Wedi et al., 2020), the use of observations related to clouds becomes increasingly relevant for model validation and improvement. The relationship between EarthCARE and NWP data can also be seen as symbiotic; the monitoring of satellite observations by comparing with the expected state of the atmosphere can be an invaluable tool for detecting and diagnosing problems before data products are released to the wider scientific community (Fielding and Janisková, 2017).

While cloud radar reflectivity and cloud lidar backscatter observations have successfully been available from space for over a decade (from the CloudSat (Stephens et al., 2002) and CALIPSO (Winker et al., 2009) satellites respectively), EarthCARE will be the first satellite cloud radar and lidar observations in near real-time and also observe radar Doppler velocity and cloud extinction directly via a cloud and aerosol optimised high-spectral resolution lidar (HSRL). In terms of radiation measuring instruments, EarthCARE will carry a multi-spectral imager (MSI) and a broadband radiometer (BBR). Expanding the diversity of EarthCARE observations that can be simulated within the ECMWF model allows the potential for a more comprehensive quality monitoring system; the potential for further direct impacts of EarthCARE observations on forecast skill to be achieved if they were to be assimilated; greater opportunities for synergistic approaches to reduce uncertainty in the observations; and facilitates the use of the additional observations in model evaluation.

In preparation for the operational monitoring and potential assimilation of these additional EarthCARE observations, the ECMWF Four-Dimensional Variational (4D-Var) assimilation was adapted in WP-4000 (Fielding and Janisková, 2022) to ingest Doppler velocity from the CPR, Rayleigh backscatter and cloud extinction in addition to cloud radar reflectivity and total lidar backscatter observations (Fig. 1.1). In WP-4000, the necessary technical developments for adding observations to the ECMWF system were made, including the 'off-line' data handling routines used for converting the raw satellite data into the format recognised by the system. Also general coding changes and additions to the 4D-Var data assimilation system itself were made and tested thoroughly. In this report, we will extend the work of WP-4000 to make a preliminary assessment of the potential for monitoring and assimilation of the additional observations.

In addition, although the observation operators were developed and coded in WP-4000, the tangent-linear (TL) and adjoint (AD) codes were constructed and tested as part of this work. While the main purpose of the TL and AD codes is to provide the gradient of the cost function within the 4D-Var minimization, they can also be used to help understand the information content of an observation by investigating the sensitivity of the output of the observation operators to its input. We will show the synergistic potential of the different EarthCARE observations within the data assimilation system and directly evaluate the sensitivities of the observations to model variables revealed by the TL/AD versions of the observation operators.

The report is organised as follows. Firstly, in Section 2, the potential information content of each observation type will be discussed with reference to the Jacobians of the observation operators, which provide the sensitivity of the simulated observations to changes in the model state. Next, the impact of the
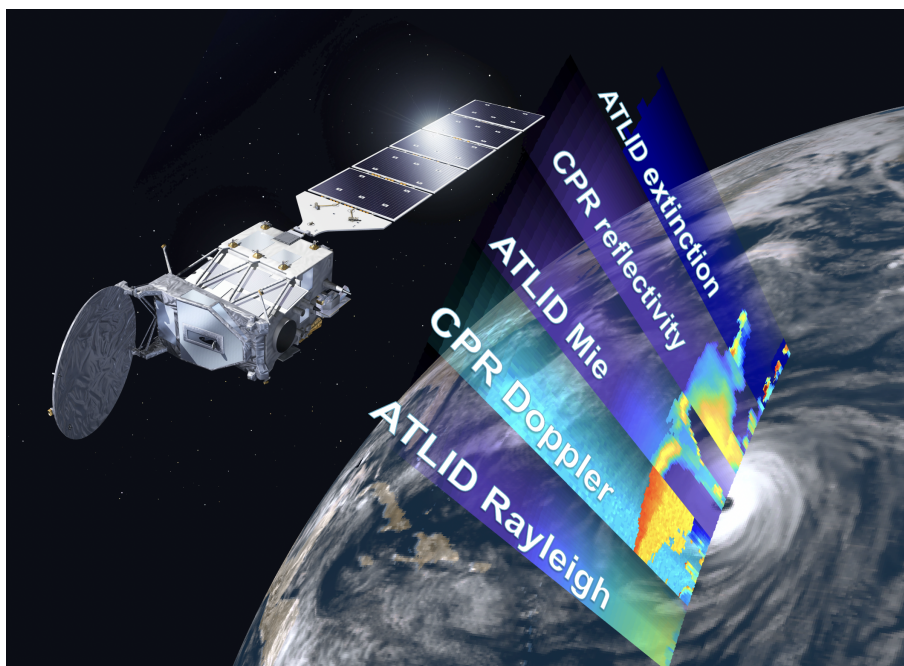
Figure 1.1: An artist's impression of the EarthCARE satellite (courtesy: ESA) superimposed on profiles of the different observation operators used in this report. The true colour image of clouds and the Earth's surface was simulated using the FLOTSAM radiance model.

new observation types will be investigated using single-cycle single-obs-type assimilation experiments in Section 3. The impact of assimilating lidar cloud extinction will be taken further in Section 4 through a one-month Observing System Experiment (OSE), where cloud extinction is included in one-month of cycling assimilation experiments. In Section 5, the potential for observation quality monitoring of MSI radiances is discussed. A summary concludes the report in Section 6.

2 Adjoint sensitivity tests of observation operators

2.1 Brief definition of tangent-linear and adjoint models

In the ECMWF data assimilation system, the 4D-Var cost function is minimized using the gradient of both the forecast model and the observation operators. To find the gradient, the adjoint (AD) version of the code is used, which itself is coded from the tangent-linear (TL) version. To build the TL model, a linearization is performed with respect to the local tangent of the model trajectory. If H is the observation operator describing the model equivalent of the observation $\mathbf{y}_M$ at any time t_i as:

$$\mathbf{y} = H[\mathbf{x}(t_i)] \tag{2.1}$$

then the sensitivity of a small perturbation $\delta\mathbf{x}$ to the model equivalent can be estimated to the first order approximating by the tangent linear model $\mathbf{H}$ (derived from the NL model H):

$$
\begin{aligned}
\delta\mathbf{y} &= \mathbf{H}[\mathbf{x}(t_i)]\delta\mathbf{x}(t_i) \\
\delta\mathbf{y} &= \frac{\partial H[\mathbf{x}(t_i)]}{\partial\mathbf{x}}\delta\mathbf{x}(t_i)
\end{aligned}
\tag{2.2}
$$

The verification of the correctness of the TL model is first performed through the classical Taylor formula:

$$\lim_{\lambda\to 0}\frac{H(\mathbf{x}+\lambda\delta\mathbf{x})-H(\mathbf{x})}{\mathbf{H}(\lambda\delta\mathbf{x})} = 1 \tag{2.3}$$

This examination of asymptotic behaviour, using perturbations the size of which becomes infinitesimally small, is performed to check the numerical correctness of the TL code.

The adjoint of a linearized operator, $\mathbf{H}$, is the linear operator, $\mathbf{H}^*$, such that:

$$\forall\mathbf{x},\forall\mathbf{y} \qquad < \mathbf{H}.\mathbf{x},\mathbf{y} >=< \mathbf{x},\mathbf{H}^*.\mathbf{y} > \tag{2.4}$$

where $<,>$ denotes the inner product and $\mathbf{x}$ and $\mathbf{y}$ are input vectors. The adjoint operator, for the simplest canonical scalar product $<,>$ (Eq. 2.4), is actually the transpose of the tangent linear operator, $\mathbf{H}^T$ (not its inverse).

For the practical verification of the adjoint code, one must test the identity described in Eq. (2.4). It is absolutely essential to ensure that the TL and AD codes verify Eq. (2.4) to the level of machine precision. Such verification was performed for all of the new observation operators and the required adjoint identity was achieved.

2.2 Using the Jacobian to highlight synergies between EarthCARE observations

In addition to being used to minimize the 4D-Var cost function, the adjoint code can be used to provide the Jacobian:

$$\mathbf{J} = \frac{\partial H(\mathbf{x})}{\partial\mathbf{x}}, \tag{2.5}$$

which gives the sensitivity of the output of the observation operator to all its input. Comparing the Jacobians of the different observation operators can highlight synergies between them. Although the adjoint technique is a more efficient method for sensitivity studies (compared with other standard approaches,

such as repetitively using the direct schemes to obtain the sensitivity of all outputs by modifying each input variable in turn) it is restricted by the tangent-linear assumption and its validity. The better the TL approximation, the more realistic and useful the sensitivity patterns are.

To investigate sensitivities of the observation operators, we first need to select a model trajectory and compute the model-equivalents about which we can linearize. Figure 2.1 shows the chosen model trajectory and model-equivalents, with profiles taken from a full 3D IFS simulation corresponding to a single CloudSat orbit from approximately 70°S to 70°N. The transect provides a wide range of cloud regimes from stratiform precipitation in profiles 550–650, with ice cloud that is well-profiled by the lidar to deep convection that contains significant attenuation of radar reflectivity in profiles 200–300.

To illustrate the difference in sensitivity between radar reflectivity and Doppler velocity, Fig. 2.2 shows their sensitivity with respect to stratiform rain for all profiles shown in Fig. 2.1 when perturbation of either radar reflectivity or Doppler velocity (i.e. gradient with respect to these quantities) of unit size at model level 80 has been provided. The output of the observation operators depend on several inputs, including temperature, humidity but predominantly on the hydrometeor content, so stratiform rain was chosen for this example. Model level 80 was chosen as it is below the freezing level for the majority of the transect.

For radar reflectivity (Fig. 2.2a), the greatest sensitivity to stratiform rain is at model level 80. This tells us that (as expected) the apparent radar reflectivity is most sensitive to the backscatter from the rain. However, there is also sensitivity to the attenuation from rain at all levels above level 80 that contain rain. There also tends to be greater sensitivity in regions with smaller rain water content in the trajectory (and hence radar reflectivity). This is because the absorption at 94 GHz depends on the rain drop size (typically greater for smaller drops; see Lhermitte (1990)). In contrast to the reflectivity, the Doppler Velocity at level 80 (Fig. 2.2b) is only sensitive to the rain water content at the same model level.

To look into more detail at the Jacobians, Fig. 2.3 shows the rain water content Jacobians for a typical deep-convection profile (profile 300 in Fig. 2.2). The sensitivity of radar reflectivity at model level 80 to rain water content is around ten times greater at the same model level than to attenuation in model levels above. Despite this, it shows that for a given radar reflectivity observation, there is some ambiguity to how the assimilation system should adjust the model to be closer to the observation. Conversely, the Doppler velocity at a given model level is only sensitive to rain water content at the given model level. Assimilating both radar reflectivity and Doppler velocity would help to remove the ambiguity in radar reflectivity between attenuation and backscatter, which should help the assimilation system to produce a more accurate analysis.

The sensitivity of the lidar operators at when either Mie backscatter or Rayleigh backscatter perturbed at level 60 to cloud ice is shown in Fig. 2.4. Level 60 was chosen as it is above the freezing level for the majority of the transect and also frequently contains cloud. For the Mie backscatter, the pattern of sensitivity to ice cloud is similar to the sensitivity of radar reflectivity to rain; there is a strong positive sensitivity at model level 60 due to the ice backscatter and a negative sensitivity in model levels above due to attenuation. Some areas of deeper ice cloud (for example profiles 200–250) lack sensitivity to attenuation due to the lidar signal being almost fully attenuated. Interestingly, in these cases, there is still sensitivity to increase the backscatter in model level 60. The sensitivity of Rayleigh backscatter to ice cloud is often very similar to the Mie backscatter, except that it does not have a strong sensitivity to the ice cloud backscatter at model level 60. The sensitivity in the ice cloud above is generally more uniform as it is not affected by cloud fraction; the Rayleigh signal has a contribution from both cloudy and clear regions. Also, given that the lidar signal is not fully attenuated, there is sensitivity to clouds above model level 60 regardless of whether there are clouds at model level 60. Finally, the sensitivity of
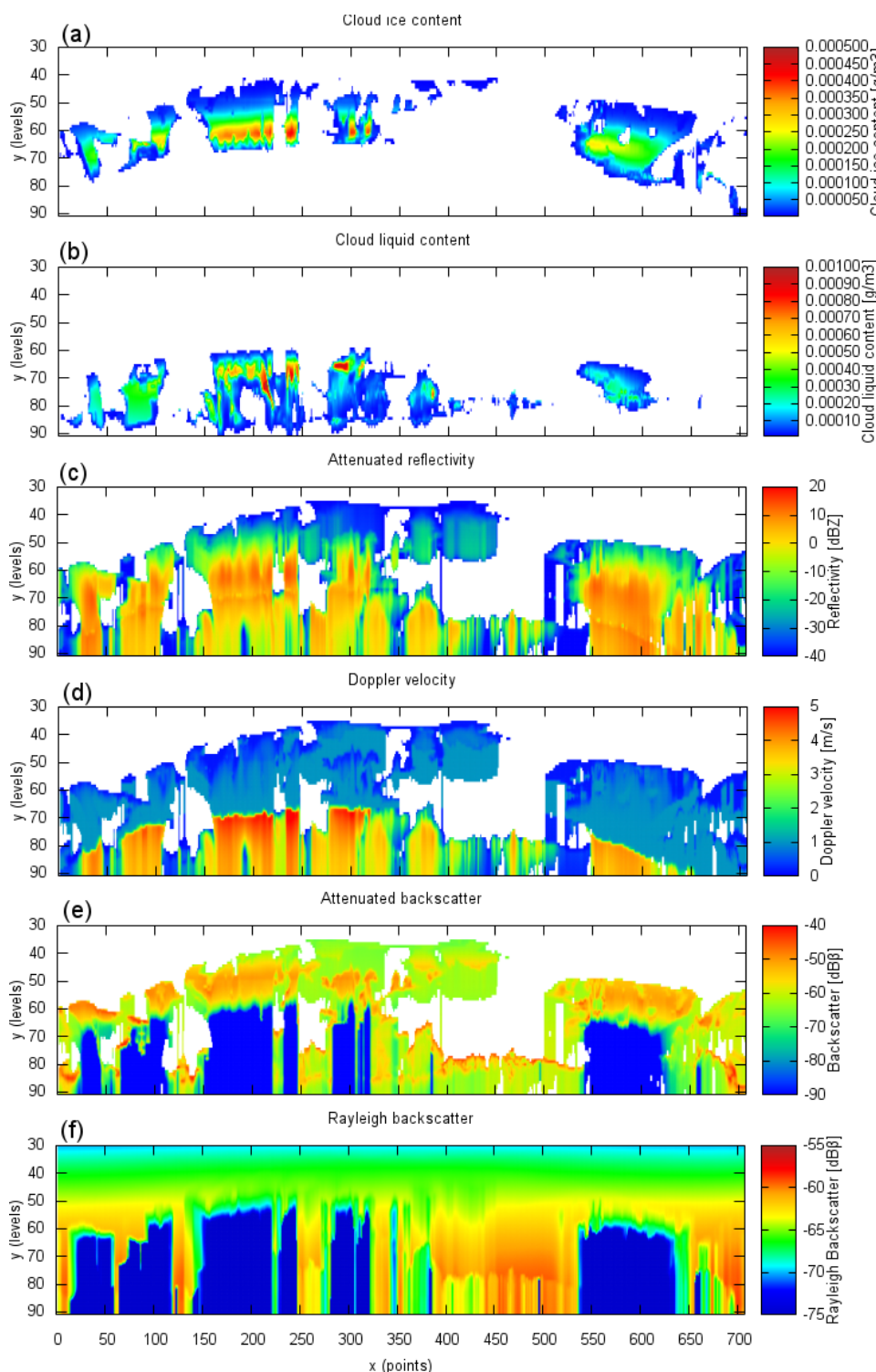
Figure 2.1: Test IFS data and model-equivalents used to evaluate tangent-linear and adjoint versions of the observation operators and their corresponding Jacobians. Panels show (a) model cloud ice content $(\mathrm{g\,m^{-3}})$, *(b) model cloud liquid water* $(\mathrm{g\,m^{-3}})$, *(c) simulated radar reflectivity (dBZ), (d) simulated Doppler velocity* $(\mathrm{m\,s^{-1}})$, *(e) simulated attenuated cloud backscatter (dBβ), (f) simulated Rayleigh backscatter (dBβ).*
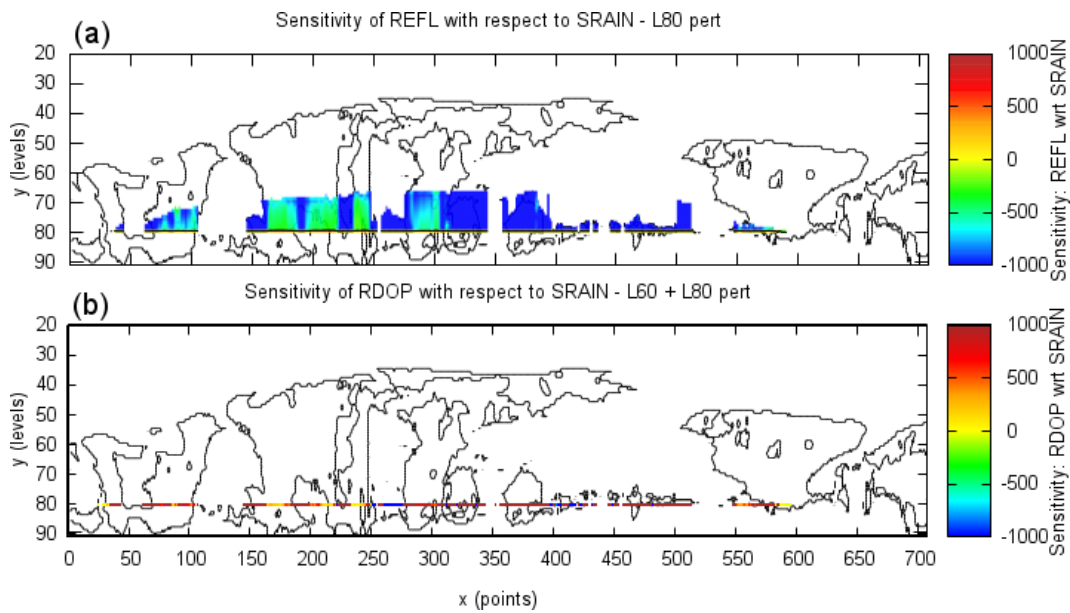
Figure 2.2: Sensitivity of (a) radar reflectivity and (b) Doppler velocity to stratiform rain profiles with units $\mathrm{dB}[\mathrm{kg/kg}]^{-1}$ *and* $\mathrm{m\,s}^{-1}[\mathrm{kg/kg}]^{-1}$ *respectively. Perturbations of either radar reflectivity or Doppler velocity (i.e. gradient with respect to these quantities) of unit size at model level 80. The corresponding trajectory is shown in Fig. 2.1.*
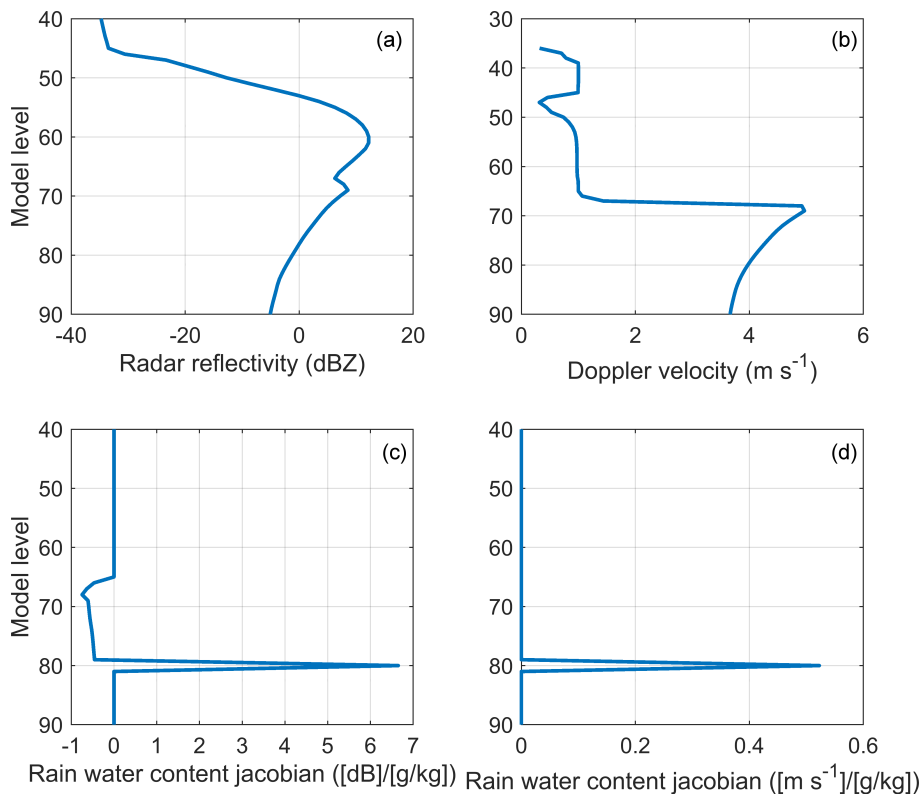

Figure 2.3: Profiles of (a) radar reflectivity, (b) Doppler velocity, together with sensitivity of (c) radar reflectivity and (d) Doppler velocity when perturbed at model level 80 to stratiform rain as in Fig. 2.2.

cloud extinction to ice water content shows the same behaviour as radar Doppler velocity to rain water; only perturbations at the level of the observation have an effect.
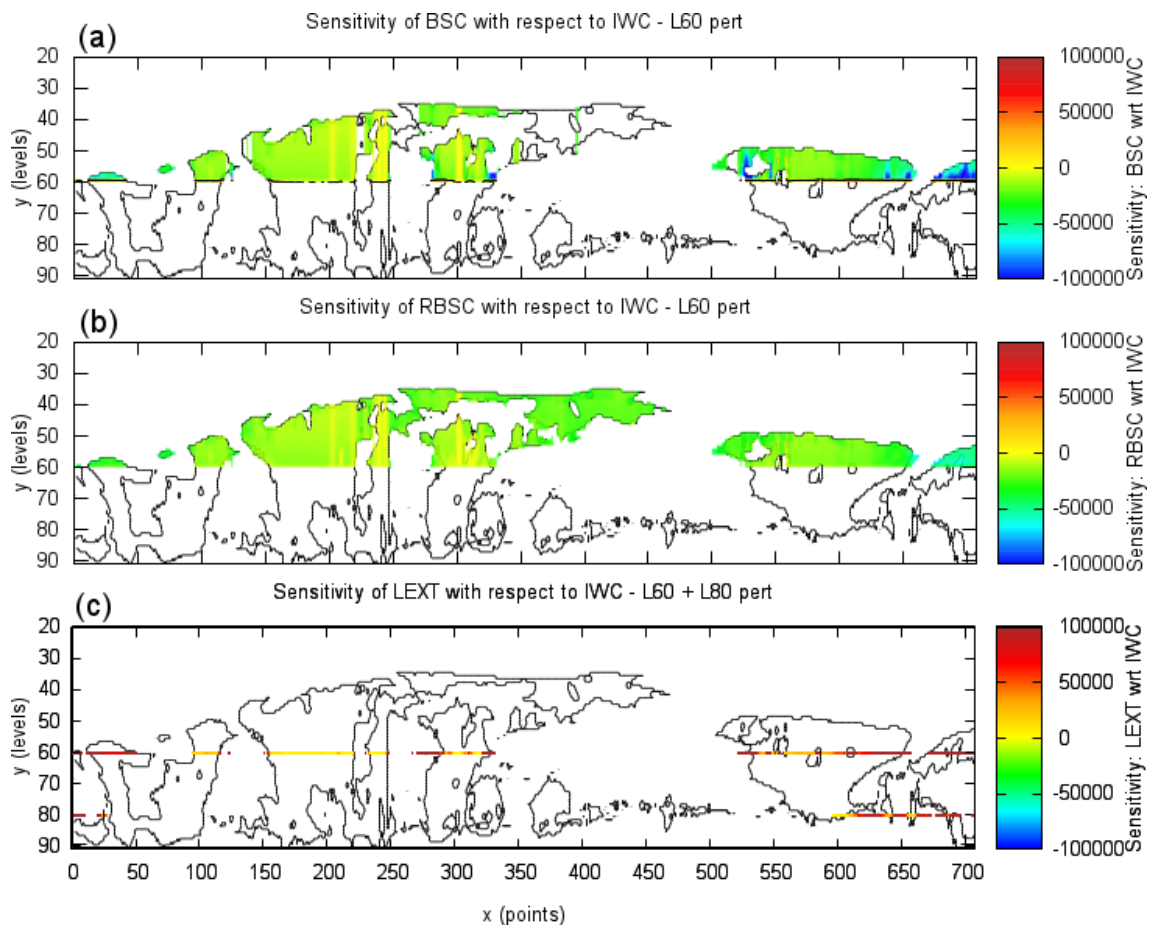

Figure 2.4: Same as Fig 2.2, but for sensitivity of (a) Mie backscatter, (b) Rayleigh backscatter, and (c) cloud extinction when perturbed at model level 60 to cloud ice profiles with units $\mathrm{dB}[\mathrm{kg/kg}]^{-1}$. *The corresponding trajectory is shown in Fig. 2.1.*

To quantify the behaviour more precisely, Fig. 2.5 shows the exact Jacobians for a typical stratiform ice cloud (model profile 600). For both Mie and Rayleigh, there is a peak in the sensitivity to ice cloud at cloud top where the particle sizes are assumed to be smallest. The sensitivity is also affected by the profile of cloud fraction in the trajectory (not shown); sensitivity tends to be less when the cloud fraction is lower because the attenuation only affects part of the model grid-box. For the Mie backscatter, the sensitivity at level 60 is roughly equal to the sensitivity in layers above; this tells us that the apparent backscatter is equally sensitive to the ice water content in layers above the observation as it is to the layer itself. Simultaneously assimilating the Rayleigh backscatter would help to remove this ambiguity as it is only sensitive to the attenuation. As cloud extinction is only sensitive to the ice water content of the observation layer itself, it would be beneficial to assimilate two out of three of the lidar observations. Given that for EarthCARE cloud extinction will be a level 2 product, it would make sense to assimilate the less-processed Mie and Rayleigh backscatter data.

When investigating the Jacobians, occasionally very large sensitivities to hydrometeor water content at the same level as the observation were found, particularly for radar reflectivity and when the hydrometeor amount in the trajectory was small (Fig. 2.6). This happens due to the non-linear relationship between
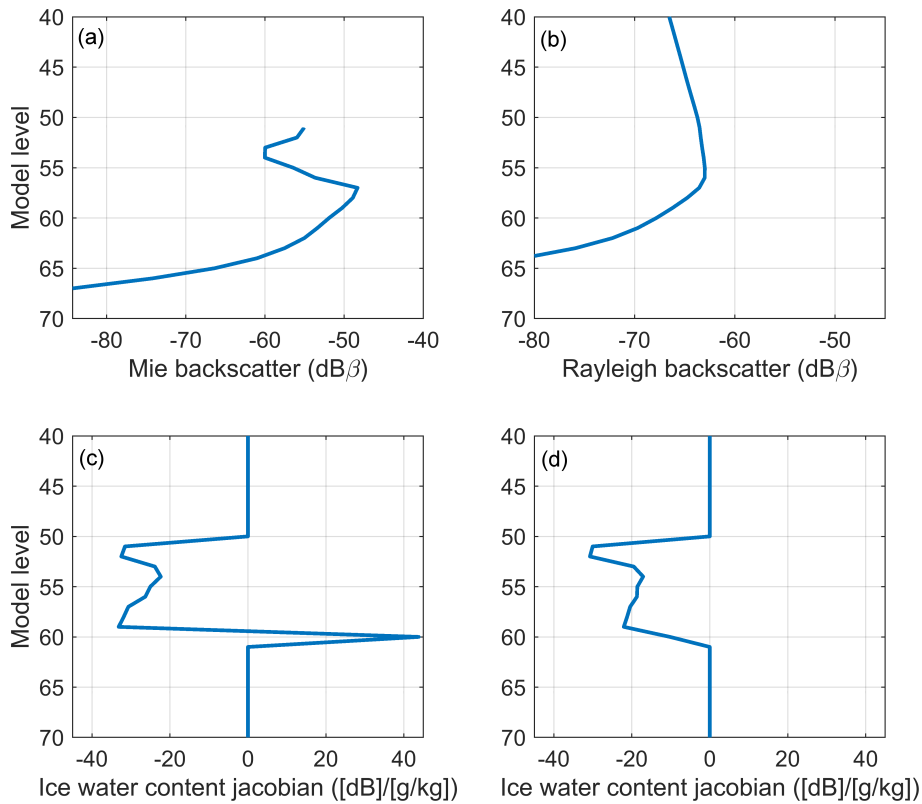
Figure 2.5: Profiles of (a) Mie backscatter, (b) Rayleigh backscatter, together with sensitivity of (c) Mie Backscatter and (d) Rayleigh backscatter when perturbed at model level 60 to ice water content as in Fig. 2.4 for profile 600.

rain water content (in linear space) and radar reflectivity (in log space); there is a large gradient for small values of water content. One way to help reduce the occurrence of these large values is to increase the 'noise factor', η, in the observation operator. Recall that the observation operator outputs radar reflectivity (and lidar backscatter) in log space:
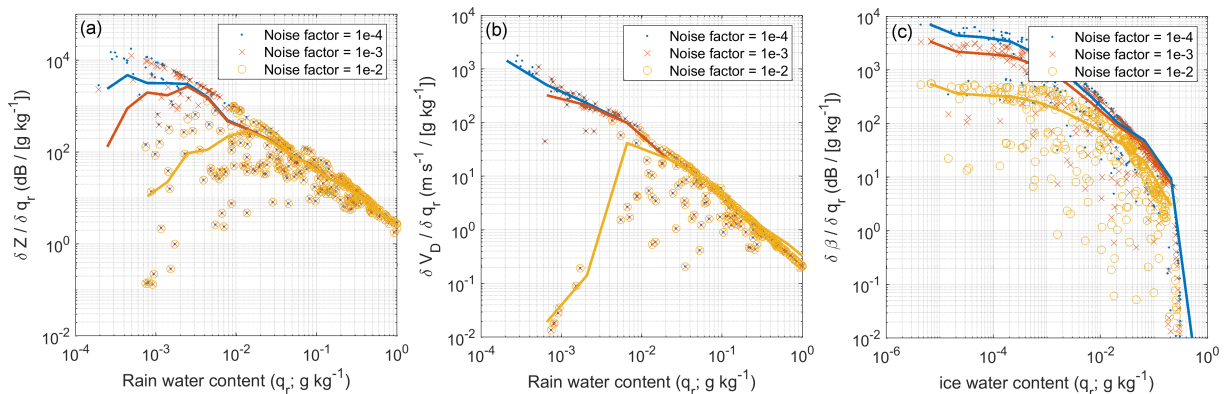
Figure 2.6: Sensitivity of (a) Radar reflectivity perturbed at model level 80 with respect to rain water content at model level 80, (b) Doppler velocity perturbed at model level 80 with respect to rain water content at model level 80 and (c) Mie backscatter perturbed at model level 60 with respect to ice water content at model level 60 using the trajectory data shown in Fig. 2.1. Each plot includes results using a noise factor of 1e-4 (blue), 1e-3 (red) and 1e-2 (yellow). Solid lines show the mean sensitivity for each noise factor.

$$Z_{dB} = 10\log_{10}(Z_{lin} + \eta) \qquad (2.6)$$

where η was included to stop very low values of radar reflectivity from causing high condition numbers in the minimization. Figure 2.6 shows that increasing the noise factor reduces the sensitivity of both radar reflectivity and Mie backscatter. The sensitivity of Doppler velocity is indirectly affected by the noise factor as Doppler velocity values are not output when the corresponding radar reflectivity is less than the noise factor. The downside of using a higher noise factor for data assimilation would be the reduced impact from observations with low radar reflectivities. An alternative approach would be to use a different transform such that the relationship between water content and radar reflectivity is more linear; one possibility could be to use the square-root of linear radar reflectivity as suggested by Hawkness-Smith and Simonin (2021) for the assimilation of rain radar reflectivity.

3   Single-cycle single-observation-type assimilation experiments

To demonstrate the performance of the different new observation types, a series of single-cycle single-observation-type 4D-Var assimilation experiments were conducted. Here we define 'single-obs-type' to mean assimilating only one observation type and 'single-cycle' to mean one 12-hour data assimilation cycle. All experiments use the same model background, so comparing the analysis increments (difference between analysis and first-guess) allows us to check the consistency in the information gained through data assimilation between the observation types.

3.1   Experiment setup

All assimilation experiments follow the same general setup as in WP-2000 (Fielding and Janisková, 2020b). The experiments all use the same background (generated using a short forecast from the operational analysis) with a 12-hour data assimilation window between 21 UTC 31st July 2007 and 9 UTC 1st August 2007. The following experiments have been run:

- **Radar reflectivity only**: using CloudSat level 2B radar reflectivity

- **Mie backscatter only**: using CALIPSO level 2 5-km C-PRO total cloud backscatter

- **Lidar extinction only**: using CALIPSO level 2 5-km C-PRO retrieved cloud extinction

- **Doppler velocity only**: using pseudo observations derived from CloudSat radar reflectivity (see WP-4000)

- **Rayleigh backscatter only**: using pseudo observations derived from CALIPSO extinction (see WP-4000)

All observations are superobbed to approximately 70 km before being assimilated. Screening is performed according to the criteria described in WP-2000 and WP-4000. Observation errors for radar reflectivity and Mie backscatter are the same as in WP-2000. Fixed observation errors of 20 dB are used for lidar extinction and $10\,\mathrm{m\,s^{-1}}$ for Doppler velocity. Rayleigh backscatter uses the same observation errors as for the Mie backscatter.

3.2 Results

Before evaluating the performance of the assimilation of the new observation types, we first evaluate the impact of assimilating the existing observation types as a reference. As shown in Fielding and Janisková (2020a), when assimilating radar reflectivity (Fig. 3.1) the data assimilation system pulls the model towards the radar observations. Note that we can see that the model has been pulled closer to the observations where the analysis increments are of the same sign and magnitude as the first guess (FG) departures. In comparison, assimilating the pseudo-observations of Doppler velocity (Fig. 3.2) also brings the model closer to the Doppler observations. For example in the deep convective rain around $-10°$N, the simulated Doppler velocity in the analysis is increased to match the pseudo-obs. However, above the melting layer in ice cloud, despite differences in the FG departures, the model cannot be pulled closer to the pseudo-obs because of the fixed sedimentation rates of ice and snow assumed by the model. Therefore the only way the simulated Doppler velocity can be adjusted is through the ratio of ice mass to snow mass.
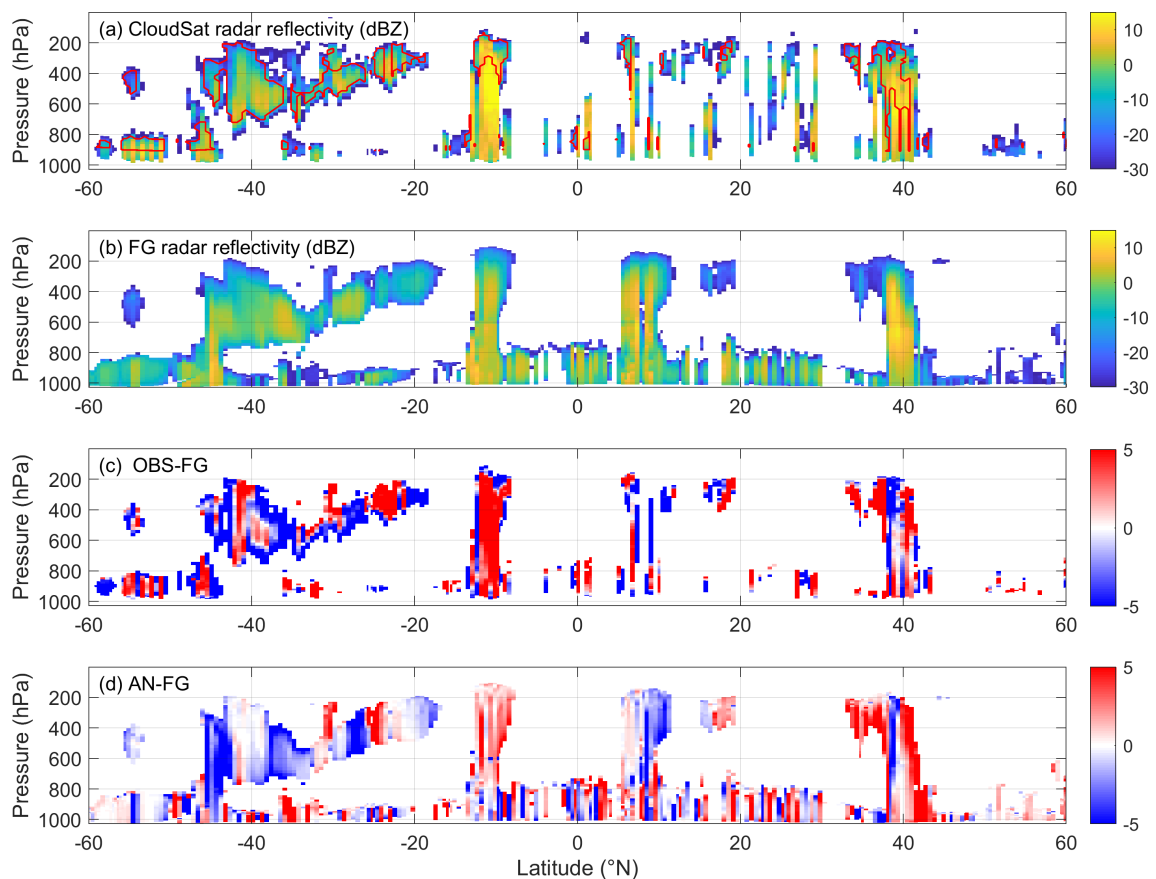

Figure 3.1: Impact of assimilating radar reflectivity in single-cycle single-obs experiments. Panels show a subset of the data assimilated, with (a) CloudSat radar reflectivity (dBZ), (b) FG radar reflectivity (dBZ), (c) first-guess departure for CloudSat radar reflectivity and (d) analysis increment in radar reflectivity (dB). The red contour in panel (a) encompasses regions that passed screening (i.e. where the observations were actively assimilated).

The assimilation of the Mie backscatter in the Mie backscatter only experiment is shown in Fig. 3.3. Comparing the Mie backscatter (Fig. 3.3a) with the radar reflectivity (Fig. 3.1a), it is clear that the Mie backscatter is inherently non-linear, which is compounded by the 70 km superobbing scale. Partly due to the variability in the observations, the FG departures (Fig. 3.3c) are noisy, which poses difficulties for a
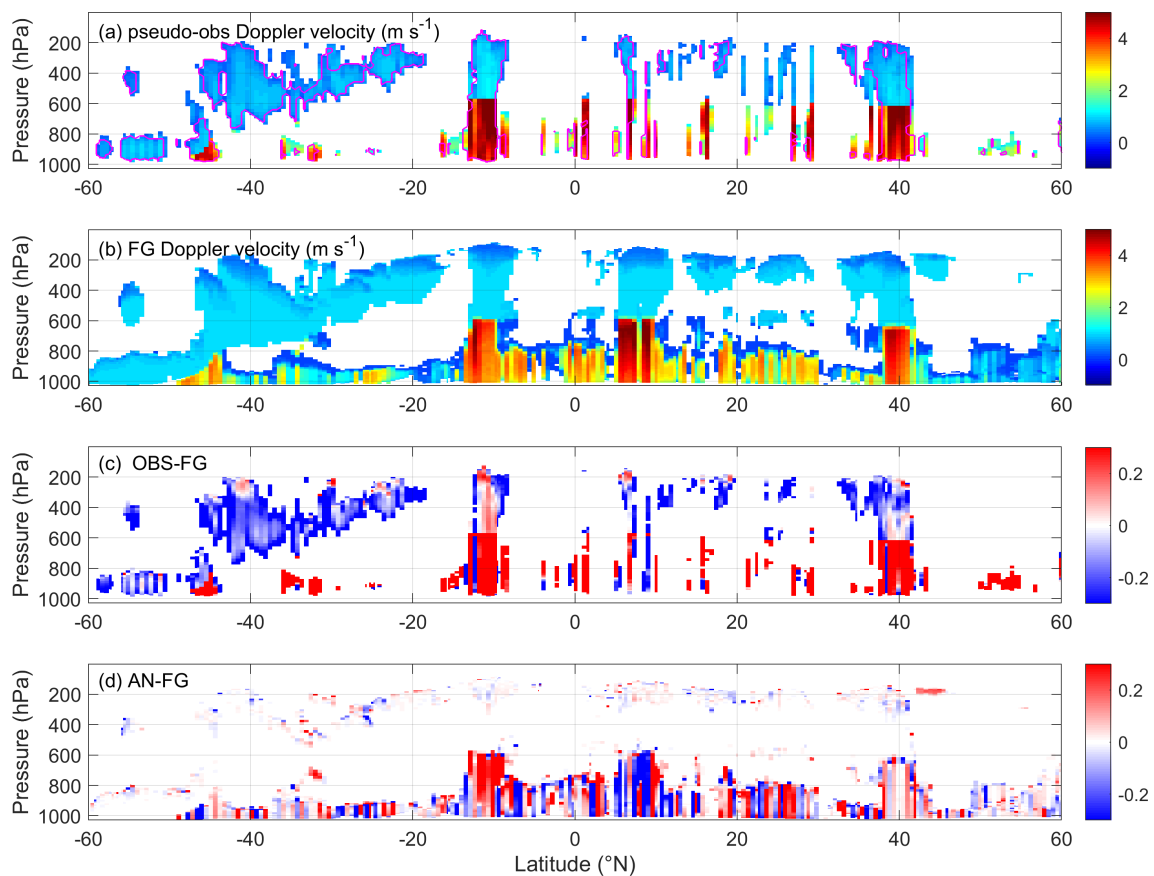
Figure 3.2: Same as Fig. 3.1, but for Doppler velocity (ms^{-1}).

4D-Var assimilation system to converge to, given the correlations in the model background. The analysis increments (Fig. 3.3d) are also noisy; as only the cloud tops tend to be assimilated it is hard to interpret the analysis increments. An example of where the model has been brought closer to the observations can be seen at the tops of the stratiform ice cloud around 40°N, where the backscatter has been increased in the analysis. The difficulties in assimilating the Mie backscatter, motivates the investigation of the assimilation of the alternative lidar observations.

Comparing Fig. 3.4a and Fig. 3.3a it is immediately clear that the Rayleigh backscatter data is generally much smoother and more continuous compared to the Mie backscatter, which should make the data more conducive to assimilation. Studying the first-guess departures (Fig. 3.4c), we can see positive (red) areas, where the model Rayleigh backscatter is less, indicating the model has too much cloud, and negative (blue) areas where the model has less cloud than the observations. Next, looking at the analysis increments (Fig. 3.4d), the model is clearly pulled towards the observations shown by the good correspondence of the analysis increments with the first-guess departures. However, there is a tendency for the model to increase backscatter below clouds, but not reduce it; the lack of sensitivity in the observation operators to moisture when there is no cloud, the so-called 'zero-gradient' problem, means that it is difficult for the assimilation system to increase cloud.

The assimilation of cloud extinction (Fig. 3.5) should be the most straight-forward as the 'observation' is a direct measure of the cloud amount. Nevertheless, the variability in the observations is similar to the Mie backscatter, suggesting non-linearity issues when averaging over the model grid-box. The variability
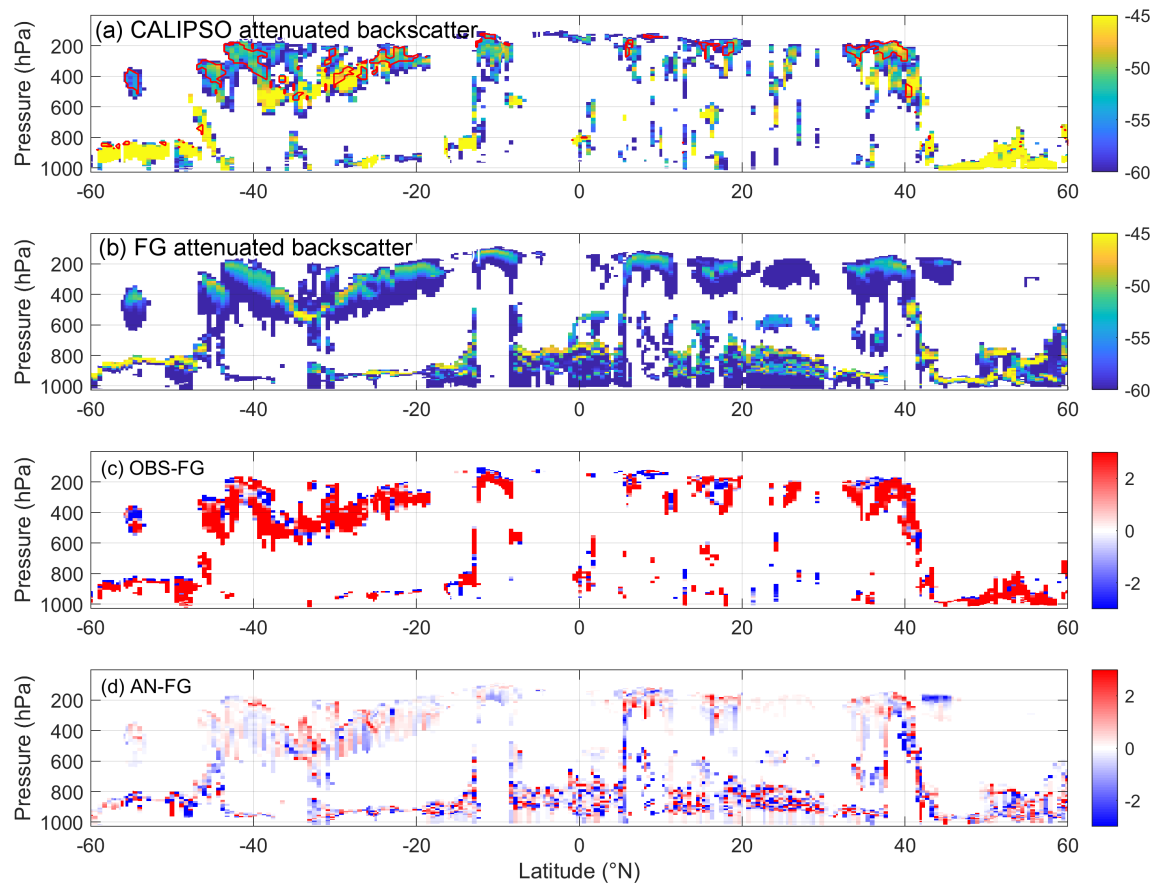
Figure 3.3: Same as Fig. 3.1, but for Mie backscatter (dBβ)

is somewhat captured in the model (Fig. 3.5b), but mostly for boundary layer clouds which are not-well retrieved in the L2 CALIPSO lidar-derived cloud extinction product. Therefore, concentrating on ice-cloud and again comparing the first-guess departures with the analysis increments, we can see that there are several regions where the data assimilation system has pulled the model towards the observations. It should be noted that the extinction screening is the same as the Mie backscatter, so only cloud tops and thin ice-cloud are actively assimilated. The data assimilation system appears to perform the best where the lidar penetrates further into the cloud, such as in the stratiform ice region between $-40°N$ and $-30°N$.

As well as evaluating the analysis increments in observation space, we can also investigate the analysis in model space. Figure 3.6 shows analysis increments of the large-scale variables temperature and relative humidity, and the cloud variables liquid and ice cloud water content for the radar reflectivity only and Doppler velocity only experiments. It is clear that assimilating radar reflectivity has a bigger overall impact on the model variables than assimilating Doppler velocity; the analysis increments of temperature and relative humidity are much greater and more wide-spread in the radar reflectivity-only experiment. As might be expected, the greatest impact of Doppler velocity is in model profiles containing significant precipitation. For example, the deep-convective cloud around $-10°N$, where the model Doppler velocity was increased by the observations, has larger increments in temperatures and humidity than in the radar reflectivity only experiment. To increase the rain rate, the model has increased the ice water content at the top of the cloud by increasing the relative humidity throughout the cloud and decreasing the temperature near the top of the cloud. The decrease in temperature below the melting layer is probably a result of
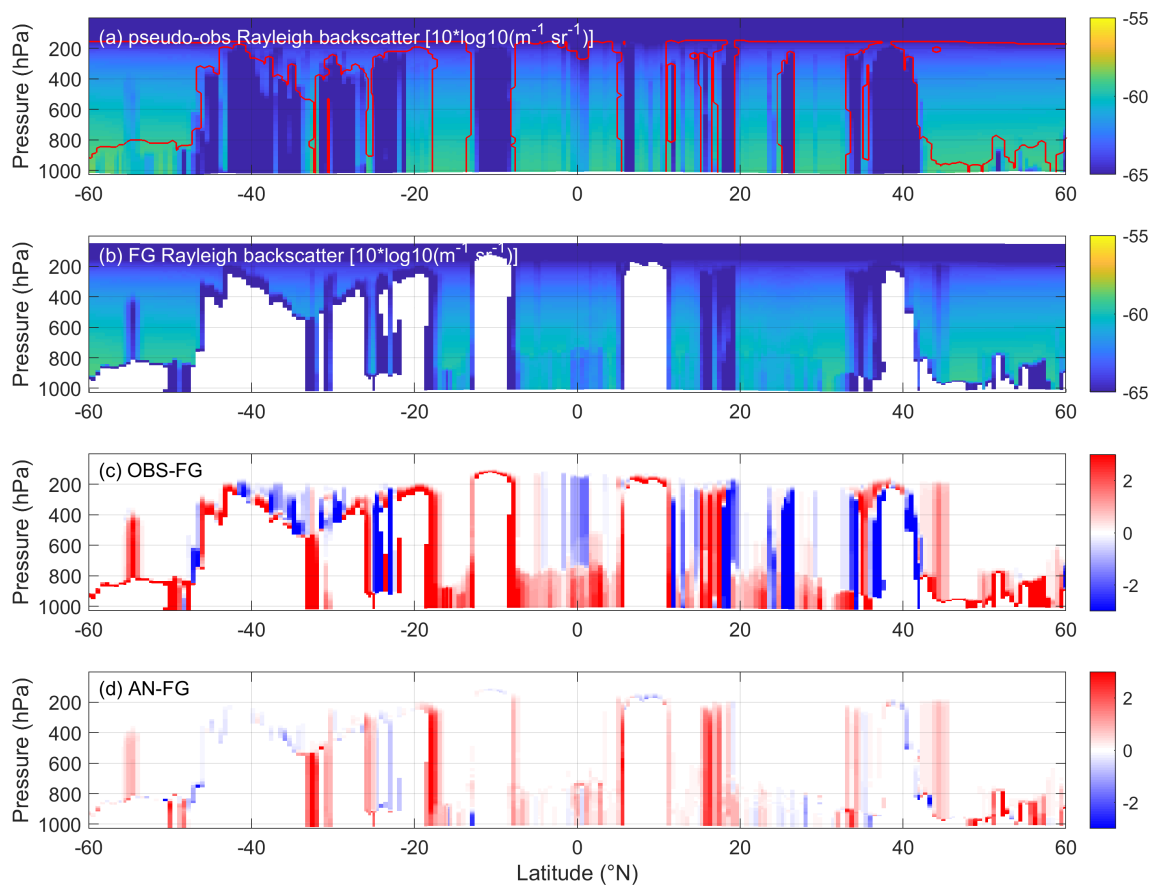
Figure 3.4: Same as Fig. 3.1, but for Rayleigh backscatter (dBβ)

increased evaporation. The noisy liquid cloud water content increments in boundary-layer clouds are due to the chaotic effect of slight changes in the initial conditions quickly causing large differences in the cloud fields rather than a direct impact of the radar variables.

Next, considering the impact of the lidar variables (Fig. 3.7 and Fig. 3.8), the Rayleigh backscatter and cloud extinction data tend to have a greater impact than the Mie backscatter. In the stratiform ice cloud region around 40°N, the impact of the Mie backscatter and lidar backscatter on model variables is remarkably similar; the increments of liquid and ice cloud water contents are broadly the same. In other regions though, the increments are different. In the ice-cloud between −30°N and −20°N, the increments in ice cloud water content for the Rayleigh backscatter experiment are closer to the increments from the radar reflectivity only experiment, suggesting that could work well together. Another feature of the Rayleigh backscatter only experiment is that the relative humidity is systematically reduced, corroborating the hypothesis that the zero-gradient problem is causing the model to systematically reduce moisture. In contrast, assimilating cloud extinction (Fig. 3.8) tends to increase the model relative humidity in these regions. Assimilating both cloud extinction and Rayleigh backscatter might help to avoid over-drying the model.

Finally, to quantify the agreement in analysis increments between the different observation types, Fig. 3.9 shows the correlation in analysis increments of model variables. The correlation between the different observation types and radar reflectivity is almost always positive for temperature, relative humidity and cloud fraction, suggesting that the assimilation of the different observation types tend to pull the model
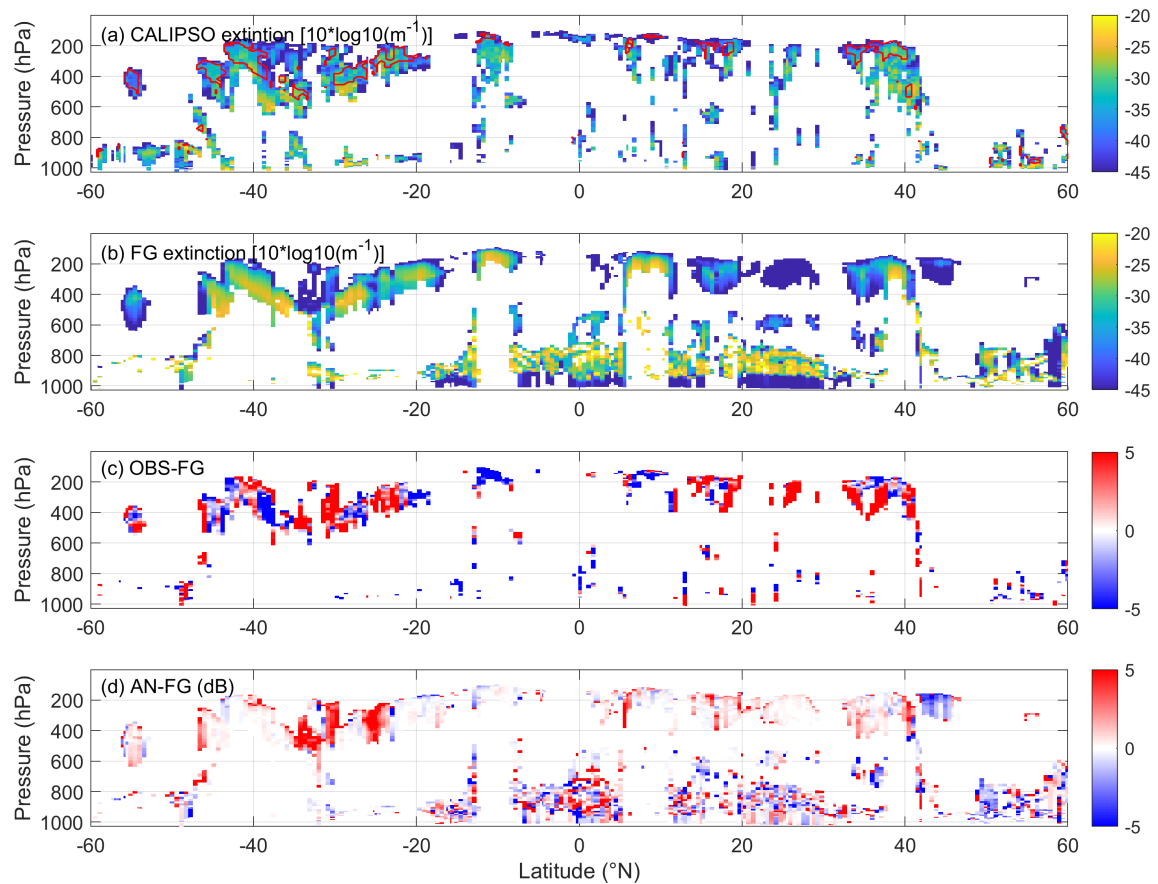
Figure 3.5: Same as Fig. 3.1, but for cloud extinction $[10\log_{10}(m^{-1})]$

in the same direction. The increments from Doppler velocity have the greatest agreement with radar reflectivity, which is perhaps not surprising given the pseudo-obs of Doppler velocity were generated from the CloudSat radar reflectivity. Comparing the increment correlations with those from the Mie backscatter also shows that the different observation types tend to agree on how to increment the model variables, but there is a much stronger correlation between the other lidar observation types than the radar variables. The greatest correlations tend be for temperature analysis increments, presumably because the background errors tend to have longer vertical correlation length scales leading to smoother analysis increments.

The evaluation of analysis increments has shown that radar reflectivity has the biggest impact on the model variables analysis, at least with the current screening and observation error specification. Rayleigh backscatter was shown to have significant potential for assimilation, but the tendency for over-drying the model needs to assessed more thoroughly. Cloud extinction also showed promise for assimilation, with the assimilation system pulling the analysis closer to the observations than it did for Mie backscatter.
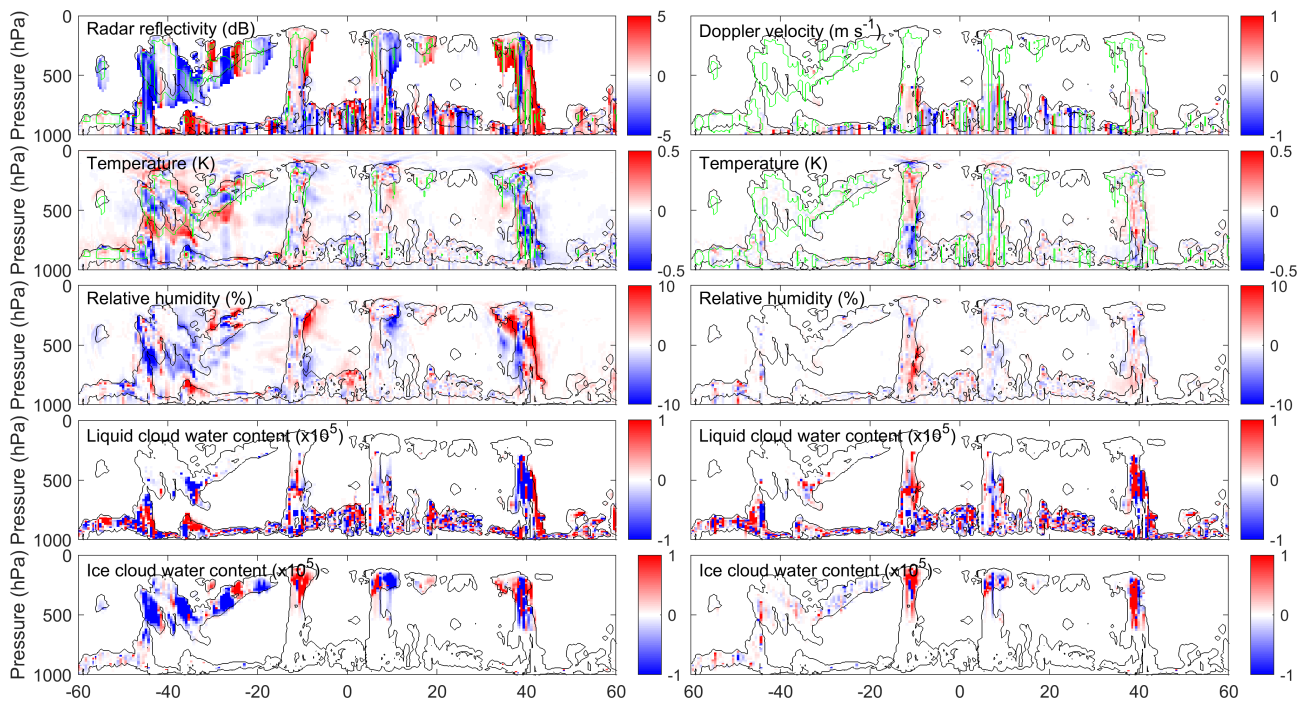
Figure 3.6: Analysis increments for (left panels) radar reflectivity and (right panels) Doppler velocity single-cycle single-obs experiments corresponding to the transects shown in Fig. 3.1 and Fig. 3.2 respectively. Panels show increments in (from top to bottom) simulated observations, temperature, relative humidity (%), liquid water content x 10^5 ($kgkg^{-1}$) and ice cloud water content x 10^5 ($kgkg^{-1}$).
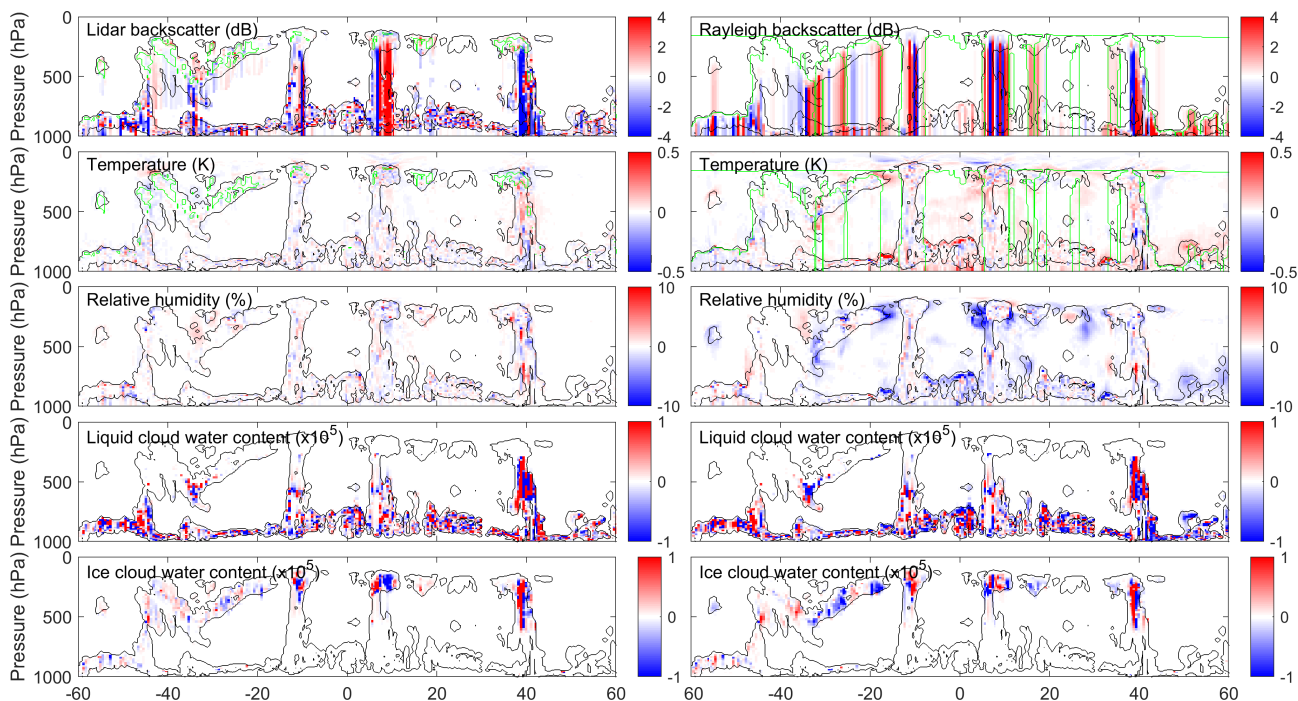
Figure 3.7: Same as Fig. 3.6, but for Mie backscatter (left) and Rayleigh backscatter (right).
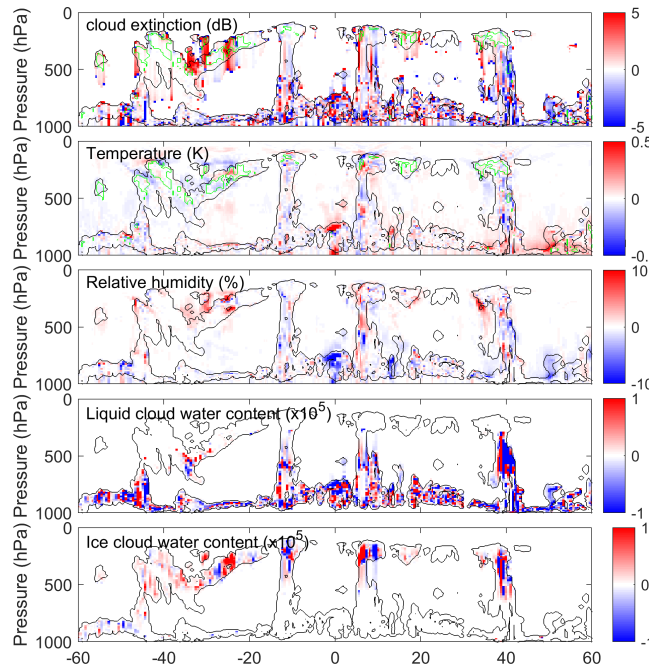
Figure 3.8: Same as Fig. 3.7, but for cloud extinction only.
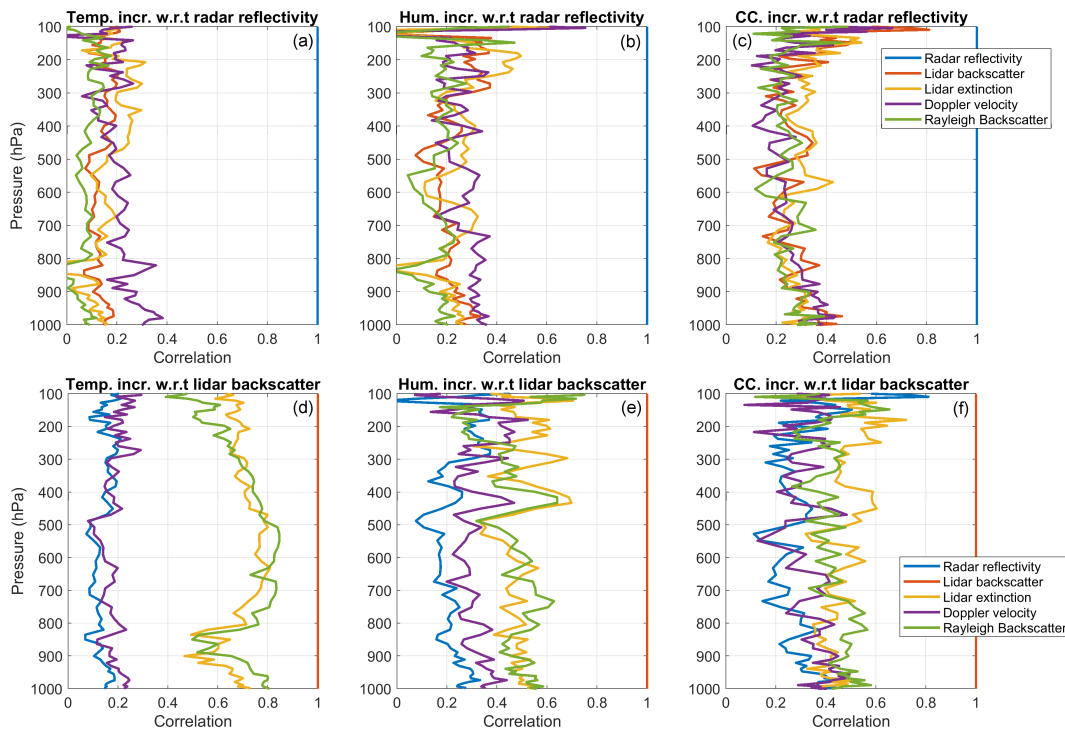
Figure 3.9: Correlations in analysis increments of (left to right) temperature, relative humidity and cloud fraction for the five different assimilation experiments (see text for details) between those generated by radar reflectivity (blue), Mie backscatter (red), Cloud extinction (yellow), Doppler velocity (purple) and Rayleigh backscatter (green) and those generated by radar reflectivity (top row) and those generated by Mie backscatter (bottom row), as a function of model pressure.

4 Impact of assimilating lidar extinction on analysis and forecast

4.1 Experimental setup

Several assimilation experiments have been run using the full system of regularly assimilated observations at ECMWF to assess the impact of assimilating cloud extinction observations using the developments described in WP-4000 (Fielding and Janisková, 2022). All experiments shown have been performed over the period of one months between 1 August 2007 and 31 August 2007 using cloud radar reflectivity from CloudSat and cloud lidar observations from CALIPSO. The results from the following experiments will be presented:

- **REF**: reference run, i.e run with all regularly assimilated observations, but without new cloud radar and lidar observations included in the 4D-Var system;
- **RL**: experiment assimilating cloud radar reflectivity and lidar backscatter observations on top of all other normally assimilated observations. All screening, observation pre-processing and observation errors are the same as in the experiments reported in WP-3000 (Fielding and Janisková, 2020c), with cloud radar reflectivity and lidar backscatter observations averaged to approximately 72 km.
- **RL+ext**: same as **RL**, but also including CALIPSO cloud extinction using the screening and quality control described in WP-4000 (Fielding and Janisková, 2022).

4.2 Impact on analysis

We begin evaluating the impact of assimilating extinction observations by assessing the impact on the observations themselves. Figure 4.1 shows the distribution of both first guess and analysis departures of cloud extinction for the **RL+ext** experiment. Looking at the results globally, we can see that the standard deviation of analysis departures is significantly smaller (13 % reduction) than the first guess departures, showing that the analysis brings the model closer to the observations. We can also see that the bias correction scheme performs well in a global sense; after bias correction, both first-guess and analysis departure distributions are symmetric and centered on zero. Having a symmetric distribution of first-guess departures suggests the screening and quality control is working well and that the observation errors are Gaussian-like (an assumption of 4D-Var).

Regionally, the greatest reduction in departures after assimilation is in the polar regions, where the standard deviation of analysis departures are around 14 % smaller than the first-guess departures. The smallest impact is in the tropics, but the analysis departures are still around 12 % smaller. In terms of the bias in the departures, a large bias correction is required in all regions, but is greatest for Southern Hemisphere mid-latitude clouds. The Antarctic region exhibits some positive skew; the right hand tail is longer suggesting some situations or regimes where the observations tend to be much greater than the model extinction.

The performance of the bias correction scheme developed in WP-4000 is evaluated in Fig. 4.2. Recall that the bias correction is a linear function of the model temperature that increases with increasing temperature trained on first guess departures for the first few days of the experiment. In a global-sense, and given that atmospheric density and temperature are strongly coupled, the bias correction performs well as a function of pressure. Regionally, the bias correction also performs well for ice cloud (pressure less than 500 hPa). In the tropics, the bias before correction is quite non-linear as a function of pressure, so is less-suited to the linear temperature-dependent bias correction. Some bias remains for all regions in
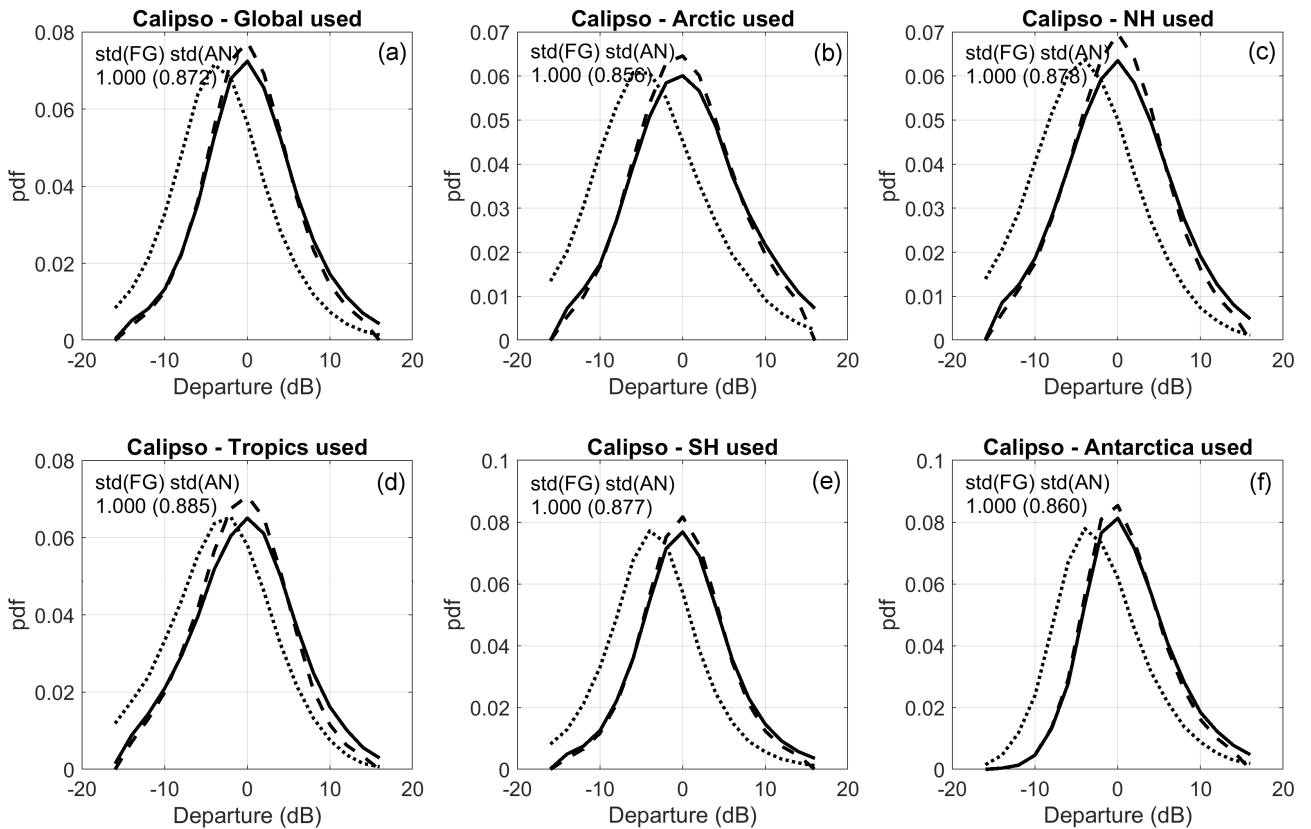
Figure 4.1: Probability density functions for first-guess before bias correction (dotted lines), first-guess after bias correction (solid lines) and analysis (dashed lines) departures for the RL+ext experiment (black) cloud lidar extinction using CALIPSO observations. Panels show results subset by region: (a) Global, (b) Arctic, (c) Northern Hemisphere, (d) Tropics, (e) Southern Hemisphere and (f) Antarctica. Also shown in the top left of each panel are the standard deviation of first guess and analysis departures, both normalised by the standard deviation of first guess departures.

clouds with pressure greater than 500 hPa due to the relative abundance of liquid clouds that have a large retrieval uncertainty in the CALIPSO cloud extinction product.

4.3 Impact on forecast

Assimilating CALIPSO extinction in addition to CloudSat radar reflectivity and CALIPSO Mie backscatter has a broadly neutral impact on the globally-averaged forecast skill of large-scale variables such as temperature, wind and humidity (Fig. 4.3) at both short- and medium-range timescales. The greatest short-term impacts are seen in the forecast skill score of vector wind at 100 hPa, where there is a 0.5 % decrease in root-mean square error, but this does not exceed the 95 % confidence interval that the impact is positive. Positive impacts of similar magnitude are seen in the forecast of mid-tropospheric temperature, but these are also not significant with 95 % confidence at a forecast lead time of 24 hours. Despite the modest impact at short lead-times, there are some signals that the reduction in errors grow into the medium-range with forecast skill improvements, particularly for geopotential and vector wind reaching a maximum at day 3-5. As found for assimilating radar reflectivity and lidar backscatter (WP-3000 Fielding and Janisková, 2020c), the impact on the forecast skill of relative humidity appears to be
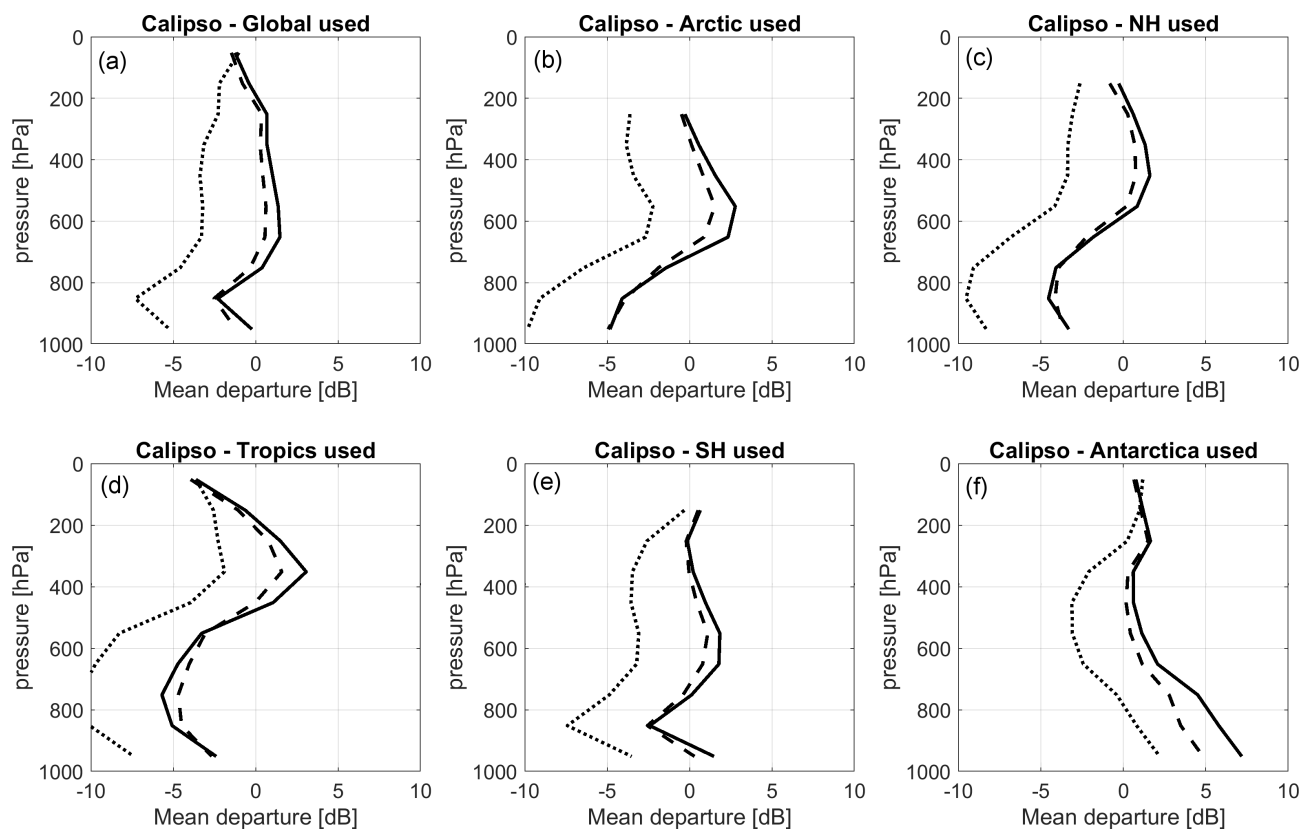
Figure 4.2: Same as Fig. 4.1, but for mean first guess after bias correction (solid), first guess before bias correction (dotted) and analysis (dashed) departures as a function of pressure (hPa).

less than the other model variables.

To understand the spatial distribution of forecast impacts at different lead times, Fig. 4.4 shows the zonal mean difference in RMS error for model temperature, wind, relative humidity and geopotential height relative to the RMS of the control experiment. For the first 12-hours of forecast, there are no significant impacts except for an increase in the forecast error of relative humidity in the Arctic lower troposphere at around 80°N. A similar signal was seen in earlier radar reflectivity and lidar backscatter assimilation experiments Janisková and Fielding (2020); Fielding and Janisková (2021a) which was removed by increasing the observation errors. A localised increase in near-surface temperature forecast errors at 75°S is also evident. At forecast lead-times of between 48 and 96 hours there are increases in forecast skill of temperature, vector wind and geopotential, mainly in the Southern Hemisphere. These improvements are beginning to show some significance in mid-tropospheric winds at 30°S. At longer lead-times, the reduction in forecast errors appears to propagate into the Southern Hemisphere stratosphere; longer assimilation experiments would help to increase the significance and give confidence in the results.

Further investigation into the increase in short-term near-surface temperature errors around 75°S revealed that the errors are localised to a relatively small section of the Antarctic ice shelf in the middle of the Southern Pacific ocean (Fig. 4.5c). A detailed analysis of individual CALIPSO extinction profiles (not shown) failed to show any obvious artefacts, so it is likely caused by assimilating extinction observations in model levels close to the surface; radar reflectivity and Mie backscatter observations are not used within 1 km of the surface due to issues with contamination from surface returns, so an obvious fix would be to also screen cloud extinction observations close to the surface. Away from the surface, spatial plots
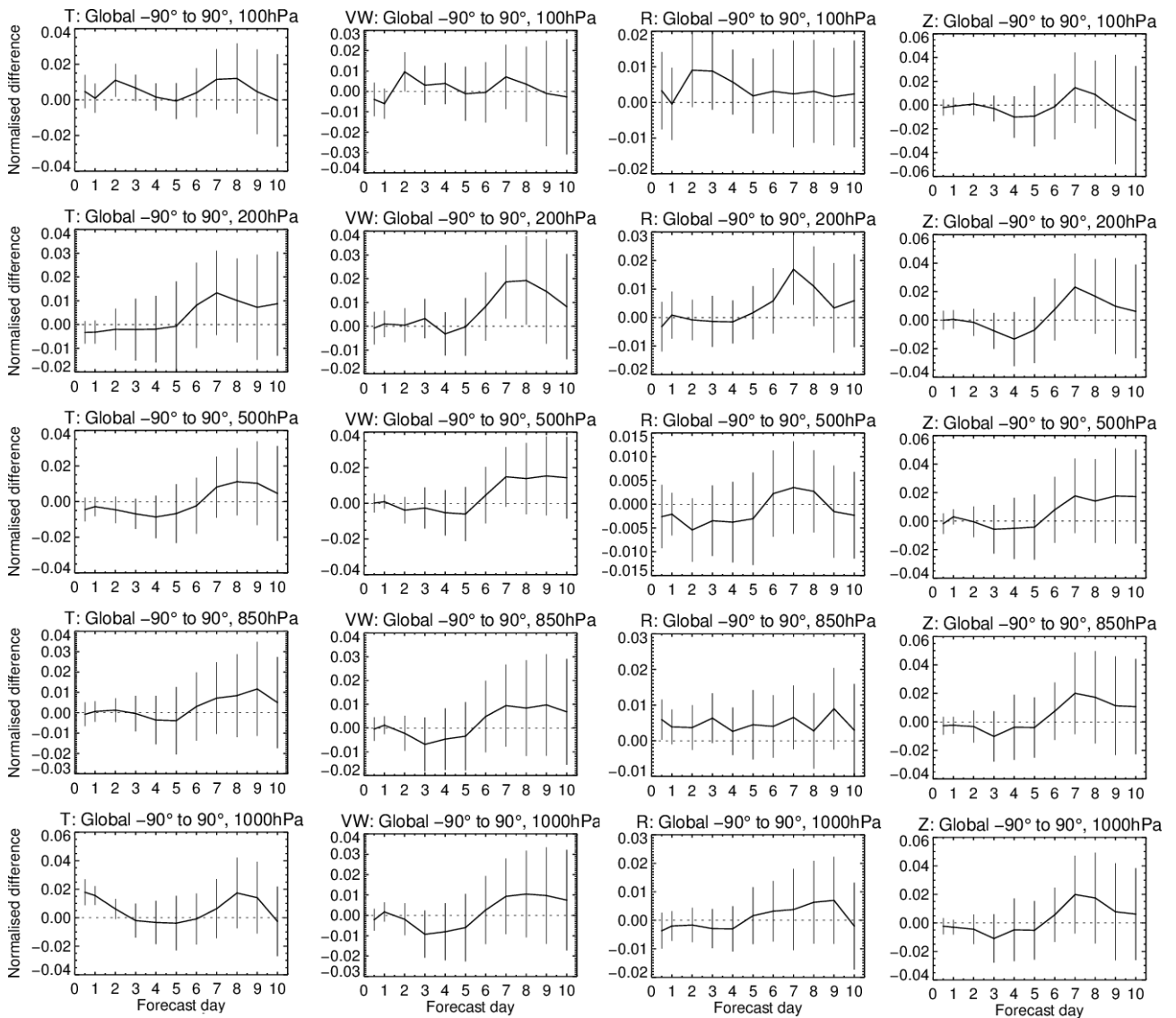
*Figure 4.3: Global mean change in root-mean squared (RMS) error of temperature (left column), vector wind (middle-left column), relative humidity (middle-right column) and relative humidity (right column) for the **RL+ext** experiment compared to own analysis, relative to the **RL** experiment. The statistics are generated from a 1-month period of assimilating CloudSat radar reflectivity and CALIPSO lidar backscatter and cloud extinction in addition to the regularly assimilated observations during August 2007. The results are shown for (from top row downwards) 100 hPa, 200 hPa, 500 hPa, 850 hPa and 1000 hPa. Error bars show 95 % confidence intervals accounting for autocorrelation and a Šidák correction for 4 independent tests.*

of various large-scale variables were generally found to be neutral, but vector-wind at 100 hPa shows signs of positive impact, particularly in the tropics (Fig. 4.5a).

Finally, the impact of assimilating cloud extinction on the first 12 hours of forecast was also evaluated by comparing the standard deviation of first-guess departures of regularly assimilated observations in the **RL+ext** experiment with those from the **RL** experiment. Most observation types showed neutral results, but a significant positive impact on the forecast skill of temperature at 500 hPa was found (Fig. 4.6). Again, longer assimilation experiments are needed to extract more significant results, but the ex-
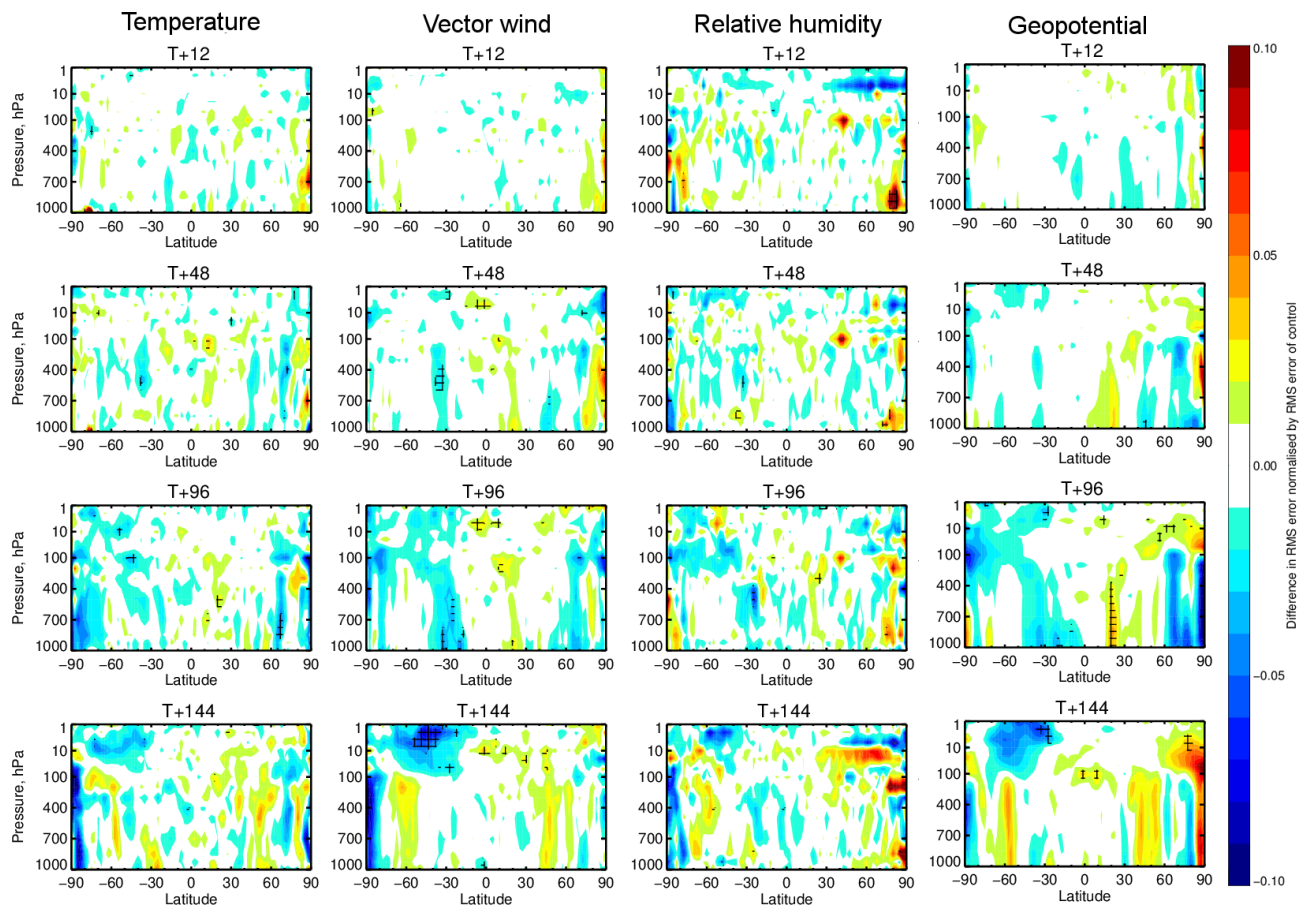
Figure 4.4: *Impact of assimilating CALIPSO cloud extinction in addition to cloud radar reflectivity and lidar backscatter from CloudSat and CALIPSO respectively on forecast skill of temperature (left column), vector wind (middle-left column), relative humidity (middle-right column) and geopotential (right column) for a 1-month period during August 2007. Panels show the zonal mean difference in root-mean-squared (RMS) error of each large-scale variable compared to own analysis, normalised by the the RMS of the* **RL** *experiment. The results are shown for forecasts at (from top row downwards) 12, 48, 96, and 144 hours. Hatched areas indicate regions that have reached 95 % confidence in the sign of the change in forecast skill from assimilating the radar and lidar observations. Blue colours indicate an improvement in forecast skill.*

periments described here show glimmers of potential for assimilating cloud extinction from EarthCARE. If further investigations into assimilating CALIPSO cloud extinction were to be carried out, it would be advisable to only actively assimilate extinction from ice cloud, as the retrievals appear to have very large biases for liquid clouds. A flow-dependent specification of the observation errors should also be used to differentiate between convective and stratiform regions, which was found to be important when assimilating radar reflectivity and Mie backscatter (Janisková and Fielding, 2020).
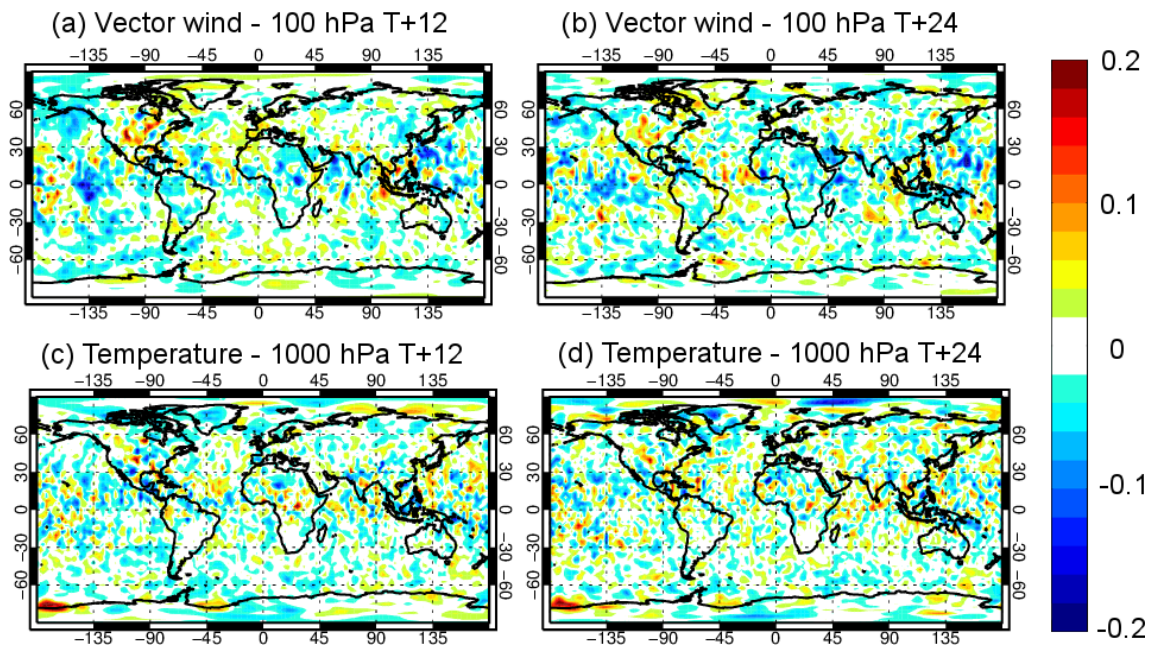
*Figure 4.5: Change in root-mean squared (RMS) error of vector wind at 100 hPa (top row) and Temperature at 1000 hPa (bottom row) relative to the **RL** experiment for forecast lead times of (left to right) 12 and 24 hours.*
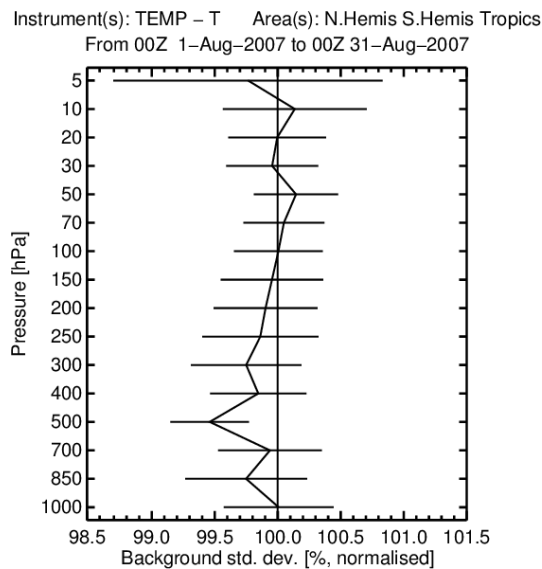
*Figure 4.6: Difference between the **RL+ext** experiment and the **RL** experiment in standard deviation normalised by the standard deviation of the **RL** experiment for the first guess fits to conventional wind observations. The **RL** experiment is represented by the 100% line and negative values correspond to improvements in the **RL+ext** experiment. Horizontal bars indicate statistical significance at the 95% level.*

5 Potential for observation quality monitoring of MSI radiances

In addition to the active instruments, CPR and ATLID, EarthCARE will host two passive instruments, the MSI and BBR (Illingworth et al., 2015). These two instruments will play a crucial part in fulfilling the EarthCARE's mission goal to achieve radiative closure in the atmosphere. Specifically, the MSI will be used to provide a vertically-integrated constraint on cloud and aerosol retrievals and to aid in the 3D construction of cloud fields for radiative closure. The BBR's main role is to provide an independent verification of broadband fluxes for the radiative closure. This section investigates the potential for observation quality monitoring of MSI radiances alongside EarthCARE's active instruments against the ECMWF model forecasts.

5.1 Radiance models

While the capability for simulating infrared and microwave radiances for either monitoring or assimilation within the IFS has been present for decades (Chevallier et al., 2004; Bauer et al., 2010), until recently, simulating solar (visible and near-infrared) radiances within data assimilation systems has not been pursued by operational forecasting centres. There are many reasons why (see Lopez et al., 2022, for a review), but the fundamental reason was a lack of a fast, differentiable radiative transfer model to use as an observation operator. Fortunately, two fast solar radiance models have recently been developed which are described here.

MFASIS

MFASIS (Method for FAst Satellite Image Synthesis) is a lookup-table based radiance model developed by Scheck et al. (2016) and is available within RTTOV (Radiative Transfer for TOVS; Saunders et al., 2018). The version of MFASIS implemented in this report (within V12.2 of RTTOV) uses an eight-dimensional radiance look-up table of: solar zenith angle, satellite zenith angle, scattering angle, surface albedo, cloud liquid optical depth, cloud liquid effective radius, ice cloud optical depth and ice cloud effective radius. The radiances for the look-up tables are computed off-line using the slow but accurate DISORT (Discrete Ordinate Method for Radiative Transfer; Stamnes et al., 1988) line-by-line radiative transfer model. Individual look-up tables are therefore required to match individual sensors' frequency bands.

FLOTSAM

In contrast to MFSAIS, the Forward-Lobe Two-Stream Radiance Model (FLOTSAM; Escribano et al., 2019) solves the radiative transfer on-line by treating the wide forward lobe of the particle scattering phase function explicitly in a separate quasi-direct stream. FLOTSAM is used in CAPTIVATE to forward model radiances, but has been revised to include the full anisotropic ice particle scattering phase functions from the Baum general-habit mixture (Baum et al., 2011). It uses the new ecCKD (Hogan and M., 2022) gas optics scheme to provide the scattering and absorption from gases. A multi-column treatment for subgrid condensate inhomogeneity is under development, but the results presented here use a single cloudy column for each radiance computation. FLOTSAM has been validated against DISORT for idealised cloud cases. Extensive validation for more complex profiles with anisotropic scattering has yet to be completed.

5.2 MFASIS vs FLOTSAM

FLOTSAM is the preferred choice for monitoring MSI radiances as its physical basis means it likely has the best accuracy in multi-layer scenes. It is also more flexible, for example to adapt to different microphysical and macrophysical assumptions. Recent work by Lopez et al. (2022) offered the opportunity to verify recent developments in FLOTSAM and also the RTTOV implementation of MFASIS. In Lopez et al. (2022), reflectance images from geostationary satellites were simulated using MFASIS and compared to observations. In Fig. 5.1 we compare reflectance images from MFASIS and FLOTSAM simulated using 9 km IFS data at 1700 UTC from a forecast initialised at 00Z on 6th September 2021. To ensure as fair a comparison as possible, MFASIS and FLOTSAM share the same surface albedo computed from a monthly mean surface BRDF (bidirectional Reflectance Distribution Function) developed by Vidot and Borbás (2014). Note there are slight differences in the bandwidths for the simulated GOES channels because the simulated GOES channels from FLOTSAM have been mapped from MODIS-like channels.

Qualitatively, the simulated reflectances from MFASIS and FLOTSAM agree well (Fig. 5.1), thus giving confidence in the processing of the model data in both MFASIS and FLOTSAM. The greatest differences can be seen in the blue channel (460 nm), where MFASIS significantly underestimates Rayleigh scattering, especially towards the limb. This is a known deficiency of MFASIS; MFASIS currently uses a fixed cloud top height in the Rayleigh scattering computations leading to an underestimation of scattering in profiles with clouds with tops lower than the assumed height. Also in the blue channel, FLOTSAM appears more reflective for most cloud types, but particularly for deep convective clouds. Intriguingly, Lopez et al. (2022) found MFASIS simulated r eflectances from the IFS to be underestimated in thick cloud situations. The first order differences in reflectances of clouds are likely to be due to different radiative scattering assumptions between MFASIS and FLOTSAM. A detailed evaluation of the different microphysical and radiative assumptions made would be required to fully explain the differences.

Despite attempting to use the same surface albedos in both radiance models, in the red channel (640 nm) there are significant differences in the apparent clear-sky reflectances; reflectances over most of Southern and Northern America are greater in FLOTSAM, while parts of Peru and Argentina are more reflective in MFASIS. In terms of clouds, boundary-layer clouds tend to be more reflective in MFASIS, while deeper clouds are more reflective in FLOTSAM. Finally, in the near-infrared channel (870 nm) and in the absence of Rayleigh scattering the differences in reflectances for different types of clouds is more obvious. Further investigation is required to understand the source of these differences.

5.3 Monitoring of along-track MODIS radiances in the A-Train

To demonstrate the potential for the monitoring of MSI radiances, MODIS radiances have been passively monitored against the ECMWF model using output from the radar and lidar assimilation experiments reported in WP-3000. As an initial demonstration, one red channel (670 nm) and one near-infrared channel (870 nm) have been monitored by matching the 3-km wide subset of MODIS radiances around the CloudSat track provided by the MODIS-AUX product for a 10 day period between 1 August 2007 and 10 August 2007. Figure 5.2 shows an example of the simulated along-track radiances before and after an assimilation that included CloudSat radar reflectivity and CALIPSO lidar backscatter on top of regularly assimilated observations. Even without assimilating the MODIS observations, the model is pulled closer to them. For example at around $-10°N$, both the CloudSat and MODIS observations are much greater than in the model FG; in the analysis, both have been pulled closer to the observations. Conversely, at around $-2°N$, the model has too much cloud in the FG, which is evident in the overestimation of
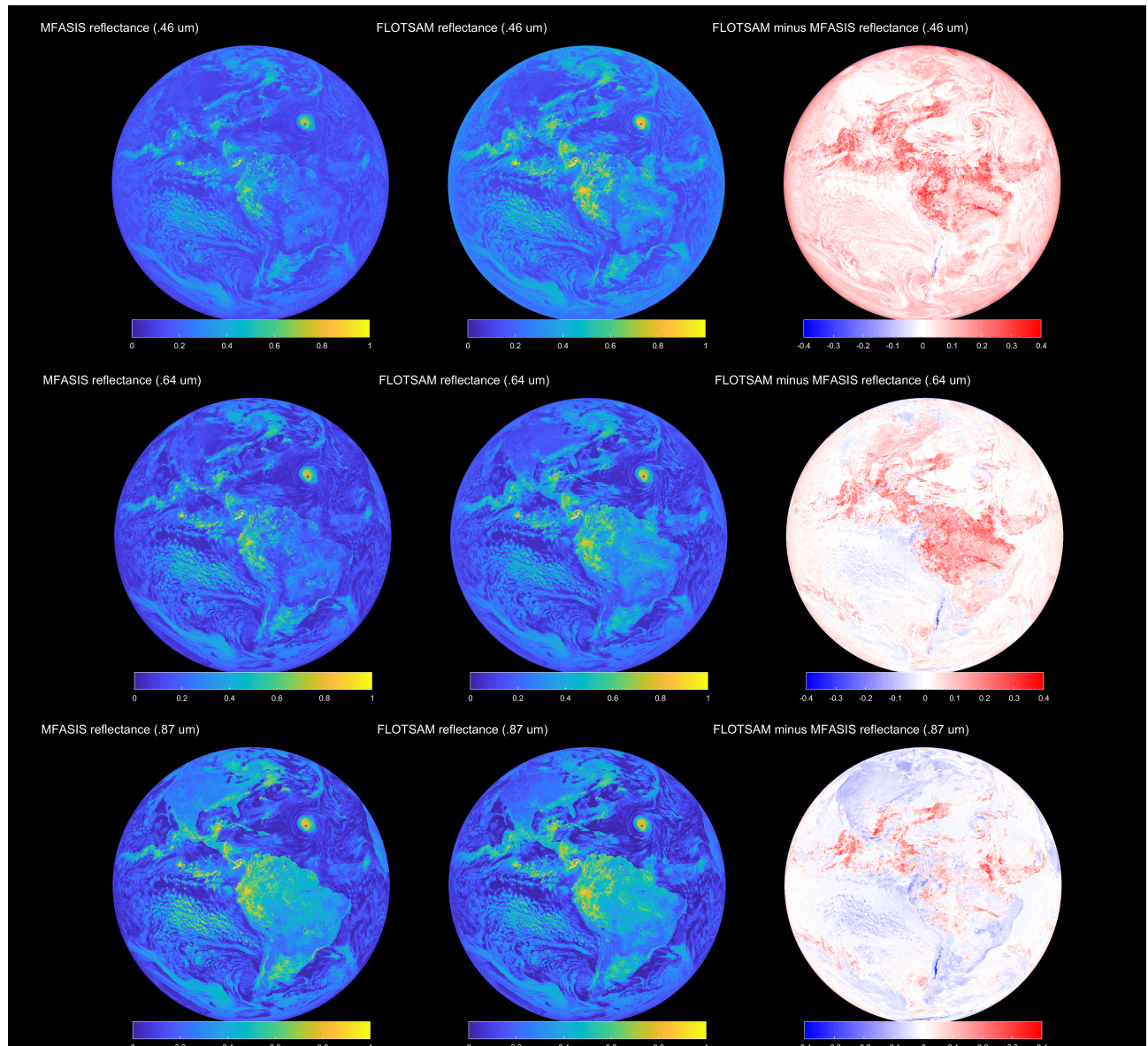
Figure 5.1: Comparison between visible and near infra-red radiances with central wavelength 460 nm (top row), 640 nm (middle row) and 870 nm (bottom row) simulated from the IFS model using MFASIS (left column), FLOT-SAM (middle column) and FLOTSAM minus MFASIS (right column) with observing geometry corresponding to the GOES-16 ABI satellite.

radar reflectivity and radiance. Again, the model analysis pulls closer to both observation types. This is not always the case, for example at around $-18°$N the model FG and AN radiances are much less the MODIS observations, despite the CloudSat radar reflectivity agreeing well with the model simulated radar reflectivity. Although the discrepancy could be caused by an incorrect cloud amount in the model, it seems more likely that the surface albedo is not reflective enough. When evaluating the MODIS FG departures it was clear that the BRDF surface albedos over land used as input to FLOTSAM are often the source of large errors, so the remainder of this investigation considers radiances over ocean only.

Statistically, when only assimilating routine observations (blue line in Fig. 5.3), the analysis tends to have root-mean-square errors that are 4 % less than the background. When also assimilating cloud radar
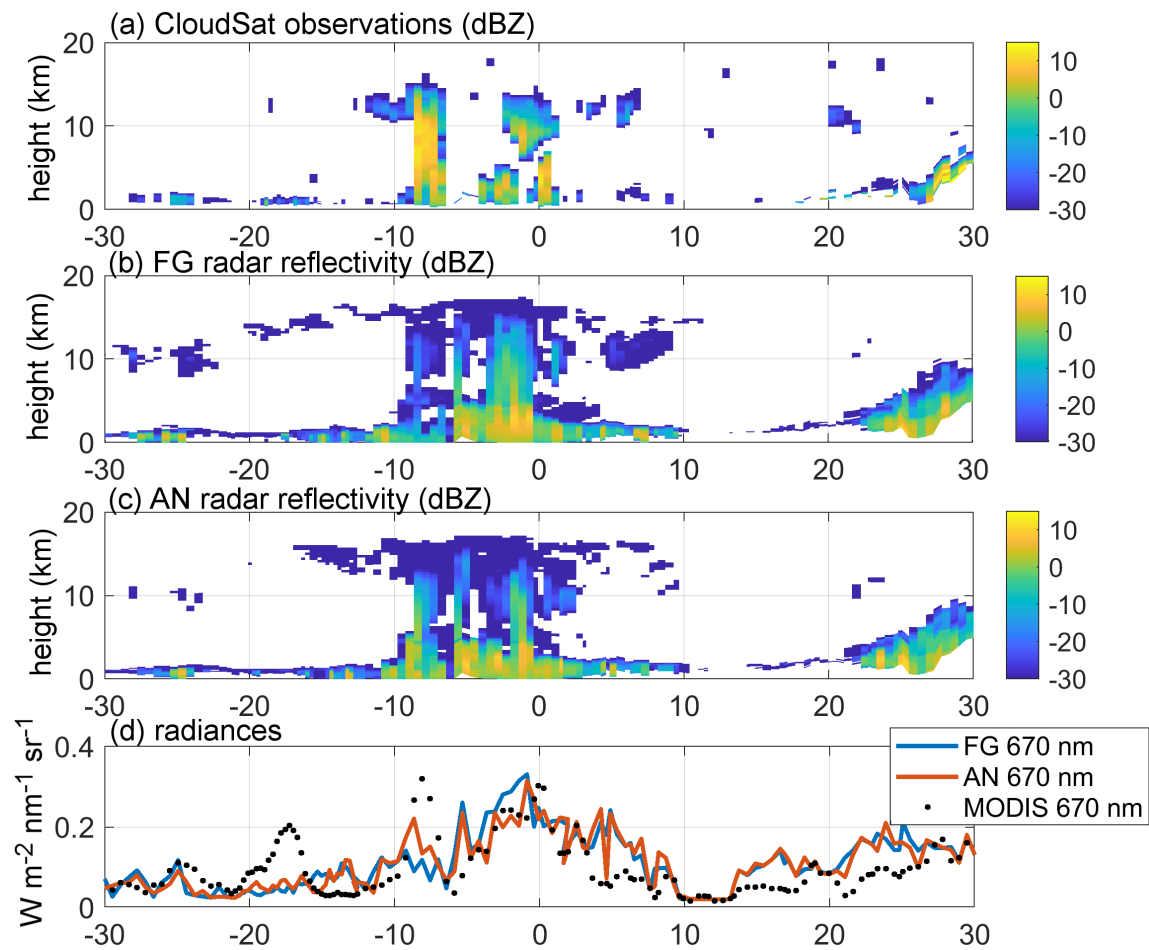
Figure 5.2: Impact of assimilation system on simulated radar reflectivity and solar radiances for a section of the A-train track within the 12 h data assimilation window between 2100 UTC 31st July 2007 and 0900 UTC 1st August 2007. Panels show (a) CloudSat radar reflectivity, (b) first-guess (FG) model radar reflectivity, (c) analysis (AN) model radar reflectivity and (d) simulated (FG; blue, AN; red) and observed (MODIS; black dots) radiances at 670 nm.

reflectivity and lidar backscatter, the analysis errors are an additional 1 % less. For ocean-only radiances, the radiances are remarkably unbiased compared to the MODIS observations and have a symmetric, Gaussian-like distribution which suggests that the radiances could be conducive to assimilation. To check that the simulated radiances are also correlated with the observations, Fig. 5.4 plots joint histograms of model and observed radiances as a function of solar zenith angle (SZA). For higher SZA, there is a clear positive correlation between the simulated and MODIS observations in both the red and near-infrared channels. However, at lower SZA the fit of model and observations becomes much noisier with increased standard deviation and reduced correlation. This decrease in correlation can be explained by the fact the lower SZA points correspond to model profiles in the tropics, whereas higher SZA points correspond to model profiles in the extra-tropics. It is well known that the IFS (and any other NWP model) struggles to represent the positioning of convective cloud that is more abundant in the tropics. This effect was also noted by Lopez et al. (2022).

The results clearly demonstrate that it is now possible to monitor MSI solar radiances against the ECMWF model. Further work should address the need for a more accurate specification of surface albedo over land; this could be achieved either through a better climatology or perhaps employing parameter estima-
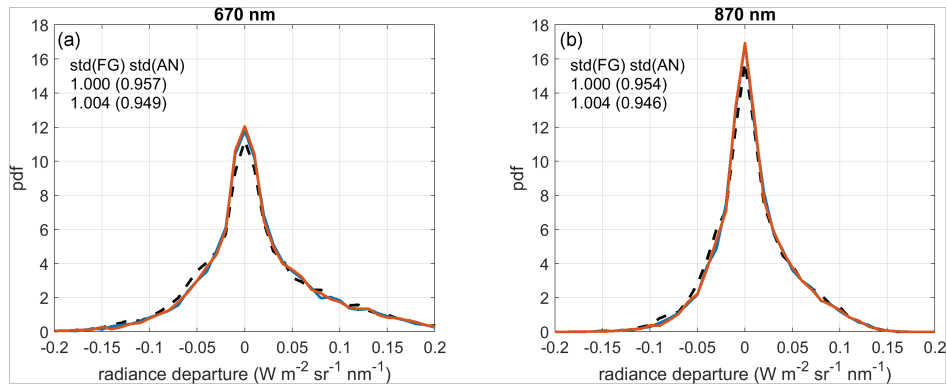
Figure 5.3: 10-day passive monitoring of MODIS radiances at (a) 670 nm and (b) 870 nm, before (FG; black dashed) and after (AN; blue, without assimilating radar reflectivity and lidar backscatter, red including radar reflectivity and lidar backscatter in the assimilation system) assimilation along the A-train track between 1 August 2007 and 10 August 2007.
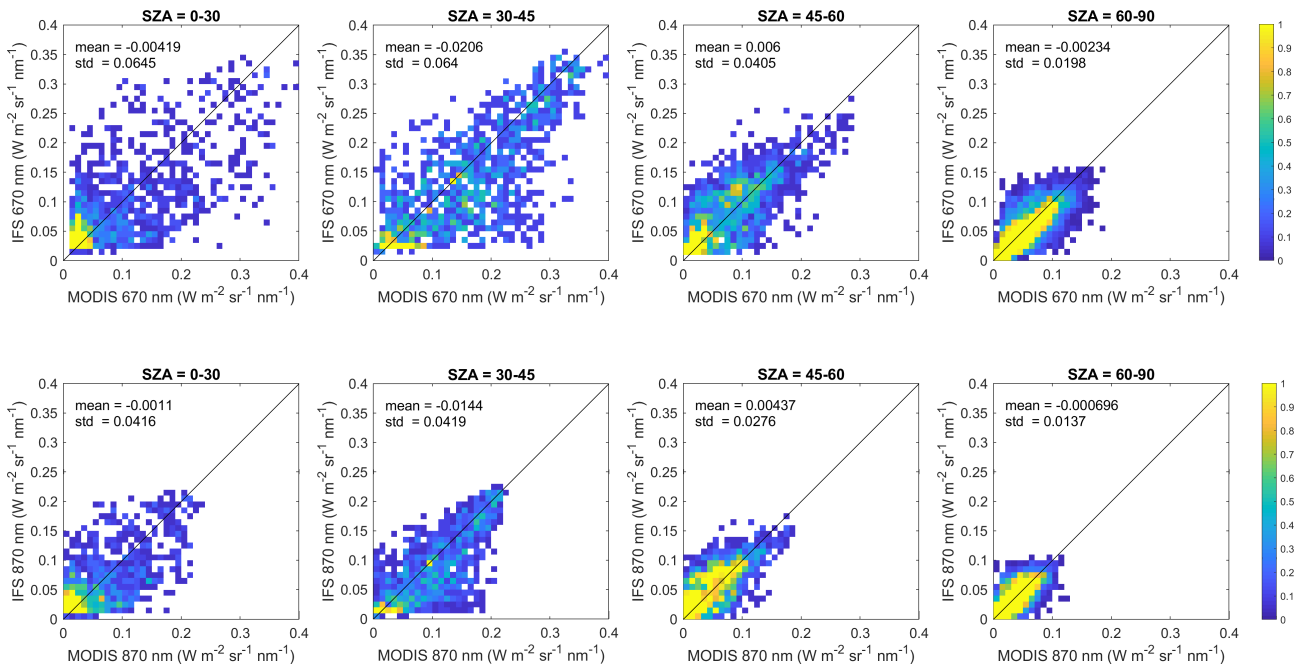

Figure 5.4: Two dimensional histograms of MODIS observed and first-guess simulated radiances at (top row) 670 nm and (bottom row) 870 nm for the 10-day monitoring of MODIS radiances against the ECMWF model along the A-train track between 1 August and 10 August 2007. Statistics are stratified by solar zenith angle (SZA) (from left to right) 0°–30°, 30°–45°, 45°–60° and 60°–90°.

tion within 4D-Var. Practically, a significant technical effort is required to adapt the assimilation system for the observation pre-processing of the MSI, including its conversion to Binary Universal FoRmat (BUFR) (see e.g., WP-4000). On the observation operator side, MFASIS is already included in the IFS via RTTOV, so it would be the obvious initial choice for simulating radiances on-line. Longer term, it is hoped FLOTSAM can also be included in RTTOV so that FLOTSAM's greater flexibility and physical realism can be leveraged.

6   Summary

This report has provided a preliminary assessment of the potential monitoring and assimilation of Earth-CARE observations in addition to cloud radar reflectivity and lidar backscatter. Building upon the developments in WP-4000, radar Doppler velocity, lidar Rayleigh backscatter, cloud extinction and solar radiances have all been evaluated. In adjoint sensitivity tests, Doppler velocity and radar reflectivity were found to have complementary information. Radar reflectivity is sensitive to both the backscatter at the model level corresponding to the observation and the attenuation from model levels above, whereas the Doppler velocity is only sensitive to the hydrometeor amount at the model level. By assimilating both observation types, it would remove ambiguity of where the model needs to change hydrometeor amount to fit the observations. Similarly for lidar, the Mie and Rayleigh backscatter show complementary sensitivities; the Rayleigh backscatter is only sensitive to attenuation in model levels above the observation, while the Mie backscatter is sensitive to both the attenuation and the backscatter of hydrometeors at the observation level. As well as investigating synergies, it was shown that the choice of transform (e.g., assimilating the observations in log space) can introduce spurious sensitivities in the TL/AD code due to extreme non-linearities. Using a larger 'noise term' as part of the variable transform was found to mitigate some of these sensitivities, but further work is required to investigate the impact of these large sensitivities and modifications.

Next, the assimilation of the additional observations was investigated through single-cycle single-obs-type 4D-Var assimilation experiments. An evaluation of analysis increments showed that radar reflectivity has the biggest impact on the model variables analysis, at least with the current screening and observation error specification. Rayleigh backscatter was showed to have significant potential for assimilation, but a tendency for over-drying the model needs to assessed more thoroughly. Cloud extinction also showed promise for assimilation, with the assimilation pulling closer to the observations than it did for Mie backscatter. The investigation of the potential for assimilation of lidar cloud extinction was taken further through one-month cycling assimilation experiments. Results were mainly neutral on forecast skill, but suggestions of positive impacts were found on the forecast of vector wind and geopotential in the Southern hemisphere extra-tropics.

Finally, the potential for monitoring of solar radiances was explored. Two radiance models, MFASIS and FLOTSAM, are now available for use to simulate solar radiances. Qualitatively, both produce similar radiances, but a comparison showed the potential for FLOTSAM to better represent Rayleigh scattering at shorter wavelengths. A demonstration of the use of monitoring solar radiances was shown by verifying the impact of assimilating cloud radar reflectivity and cloud lidar backscatter on MODIS radiances. Compared to a control experiment, assimilating CloudSat radar reflectivity and CALIPSO lidar backscatter brought model simulated radiances from the analysis closer to MODIS radiances by around 1 %.

Acknowledgments

List of Acronyms

4D-Var	Four-Dimensional Variational Assimilation
AD	ADjoint
AN	Analysis
ATLID	ATmospheric LIDar
BBR	BroadBand Radiometer
BRDF	Bidirectional Reflectance Distribution Function
BUFR	Binary Universal Form for the Representation of meteorological data
C-PRO	Cloud profiling radar PROcessing
CALIOP	Cloud-Aerosol Lidar with Orthogonal Polarization
CALIPSO	Cloud-Aerosol Lidar and Infrared Pathfinder Satellite Observation
CAPTIVATE	Cloud and Aerosol Property reTrIeval using a VAriational TEchnique
CKD	correlated k-distribution method
CloudSat	NASA's cloud radar mission
CPR	Cloud Profiling Radar
DISORT	Discrete Ordinate Method for Radiative Transfer
EarthCARE	Earth, Clouds, Aerosols and Radiation Explorer
ecCKD	ECMWF tool for generating fast CKD gas optics model
ECMWF	European Centre for Medium Range Weather Forecasts
ESA	European Space Agency
FG	First Guess
FLOTSAM	Forward-Lobe Two-Stream Radiance Model
GOES	Geostationary Operational Environmental Satellite
HSRL	High-Spectral Resolution Lidar
IFS	Integrated Forecasting System of ECMWF
MFASIS	Method for FAst Satellite Image Synthesis
MODIS	Moderate Resolution Imaging Spectroradiometer
MSI	Multi-Spectral Imager
NASA	National Aeronautics and Space Administration
NL	Non-Linear
NWP	Numerical Weather Prediction
OBS	OBServations
ODB	Observation Data Base
OSE	Observing System Experiment
RTTOV	Radiative Transfer for TOVS
TIROS	Television InfraRed Observation Satellite
SZA	Solar Zenith Angle
TL	Tangent Linear
TOVS	TIROS Operational Vertical Sounder
UTC	Universal Time Coordinated
WP	Work Package

References

Bauer, P., A. Geer, P. Lopez, and D. Salmond, 2010: Direct 4D-Var assimilation of all-sky radiances. Part I: Implementation, *Q. J. R. Meteorol. Soc.*, **136**, 1868—-1885, doi:10.1002/qj.659.

Baum, B. A., P. Yang, A. J. Heymsfield, C. G. Schmitt, Y. Xie, A. Bansemer, Y.-X. Hu, and Z. Zhang, 2011: Improvements in shortwave bulk scattering and absorption models for the remote sensing of ice clouds, *Journal of Applied Meteorology and Climatology*, **50**(5), 1037–1056.

Chevallier, F., P. Lopez, A. Tompkins, M. Janisková, and E. Moreau, 2004: The capability of 4D-Var systems to assimilate cloud-affected satellite infrared radiances, *Q. J. R. Meteorol. Soc.*, **130**, 917–932.

Escribano, J., A. Bozzo, P. Dubuisson, J. Flemming, R. J. Hogan, L. C.-Labonnote, and O. Boucher, 2019: A benchmark for testing the accuracy and computational cost of shortwave top-of-atmosphere reflectance calculations in clear-sky aerosol-laden atmospheres, *Geoscientific Model Development*, **12**(2), 805–827.

Fielding, M. and M. Janisková, 2020a: Direct 4D-Var assimilation of space-borne cloud radar and lidar observations. Part I: Observation operator and implementation, *Q. J. R. Meteorol. Soc.*, **146**(733), 3877–3899.

Fielding, M. and M. Janisková, 2020b: Optimisation of observation impact on analysis, WP-2000 report for the project Preparations for EarthCARE Assimilation - Radar and Lidar Cloud Observations (PEARL Cloud), ESA ESTEC contract 4000128669/19/NL/CT.

Fielding, M. and M. Janisková, 2020c: Optimisation of observation impact on forecasts, WP-3000 report for the project Preparations for EarthCARE Assimilation - Radar and Lidar Cloud Observations (PEARL Cloud), ESA ESTEC contract 4000128669/19/NL/CT.

Fielding, M. and M. Janisková, 2021a: Optimisation of observation impact on forecast, WP-3000 report for the project Preparations for EarthCARE Assimilation - Radar and Lidar Cloud Observations (PEARL Cloud) to ESA ESTEC, contract 4000128669/19/NL/CT, 34 pp.

Fielding, M. and M. Janisková, 2022: Assimilation system development for additional observations, WP-4000 report for the project Preparations for EarthCARE Assimilation - Radar and Lidar Cloud Observations (PEARL Cloud), ESA ESTEC contract 4000128669/19/NL/CT.

Fielding, M. D. and M. Janisková, 2017: Observation quality monitoring and pre-processing, WP-2000 report for the project Operational Assimilation of Space-borne Radar and Lidar Cloud Profile Observations for Numerical Weather Prediction, 4000116891/16/NL/LvH, pp.

Hawkness-Smith, L. D. and D. Simonin, 2021: Radar reflectivity assimilation using hourly cycling 4d-var in the met office unified model, *Quarterly Journal of the Royal Meteorological Society*, **147**(736), 1516–1538.

Hogan, R. J. and M. M., 2022: A tool for generating fast k-distribution gas-optics models for weather and climate applications, *Journal of Advanced Modeling Earth Systems., in review*.

Illingworth, A. et al., 2015: The earthcare satellite: The next step forward in global measurements of clouds, aerosols, precipitation, and radiation, *Bulletin of the American Meteorological Society*, **96**(8), 1311–1332.

Janisková, M. and M. Fielding, 2020: Direct 4D-Var assimilation of space-borne cloud radar cloud radar reflectivity and lidar backscatter. Part II: Impact on analysis and subsequent forecast, *Q. J. R. Meteorol. Soc.*, **146(733)**, doi:10.1002/qj.3879,3900–3916.

Lhermitte, R., 1990: Attenuation and scattering of millimeter wavelength radiation by clouds and precipitation, *Journal of Atmospheric and Oceanic Technology*, **7**(3), 464 – 479.

Lopez, P., M. Matricardi, and M. Fielding, 2022: Validation of ifs+rttov/mfasis solar reflectances against goes-16 abi obs, Ecmwf tech memo 892.

Saunders, R., J. Hocking, E. Turner, P. Rayer, D. Rundle, P. Brunel, J. Vidot, P. Roquet, M. Matricardi, A. Geer, et al., 2018: An update on the rttov fast radiative transfer model (currently at version 12), *Geoscientific Model Development*, **11**(7), 2717–2737.

Scheck, L., P. Frerebeau, R. Buras-Schnell, and B. Mayer, 2016: A fast radiative transfer method for the simulation of visible satellite imagery, *Journal of Quantitative Spectroscopy and Radiative Transfer*, **175**, 54–67.

Stamnes, K., S.-C. Tsay, W. Wiscombe, and K. Jayaweera, 1988: Numerically stable algorithm for discrete-ordinate-method radiative transfer in multiple scattering and emitting layered media, *Applied optics*, **27**(12), 2502–2509.

Stephens, G., D. Vane, R. Boain, G. Mace, K. Sassen, Z. Wang, A. Illingwort, E. O'Connor, W. Rossow, and S. Durden, 2002: The CloudSat mission and the A-train, *Bull. Am. Meteorol. Soc.*, **83(12)**, 1771–1790.

Vidot, J. and E. Borbás, 2014: Land surface vis/nir brdf atlas for rttov-11: model and validation against seviri land saf albedo product, *Quarterly Journal of the Royal Meteorological Society*, **140**(684), 2186–2196.

Wedi, N. P., I. Polichtchouk, P. Dueben, V. G. Anantharaj, P. Bauer, S. Boussetta, P. Browne, W. Deconinck, W. Gaudin, I. Hadade, S. Hatfield, O. Iffrig, P. Lopez, P. Maciel, A. Mueller, S. Saarinen, I. Sandu, T. Quintino, and F. Vitart, 2020: A baseline for global weather and climate simulations at 1 km resolution, *Journal of Advances in Modeling Earth Systems*, **12**(11), e2020MS002192, e2020MS002192 10.1029/2020MS002192.

Winker, D., M. Vaughan, A. Omar, Y. Hu, K. Powell, Z. Liu, W. Hunt, and S. Young, 2009: Overview of the CALIPSO mission and CALIOP data processing algorithms, *J. Atmos. and Ocean. Tech.*, **26(7)**, 2310–2323.